

Photoionized Herbig-Haro objects in the Orion Nebula through deep high-spectral resolution spectroscopy II: HH 204

J. E. MÉNDEZ-DELGADO ,^{1,2} C. ESTEBAN ,^{1,2} J. GARCÍA-ROJAS ,^{1,2} W. J. HENNEY ,³ A. MESA-DELGADO ,⁴ AND K. Z. ARELLANO-CÓRDOVA 

¹*Instituto de Astrofísica de Canarias (IAC), E-38205 La Laguna, Spain*

²*Departamento de Astrofísica, Universidad de La Laguna, E-38206 La Laguna, Spain*

³*Instituto de Radioastronomía y Astrofísica, Universidad Nacional Autónoma de México, Apartado Postal 3-72, 58090 Morelia, Michoacán, Mexico*

⁴*Calle Camino Real 64, Icod el Alto, Los Realejos, 38414, Tenerife, Spain*

⁵*The University of Texas at Austin, 2515 Speedway Boulevard Stop C1400, Austin, TX 78712, USA*

(Received XXX; Revised YYY; Accepted ZZZ)

Submitted to ApJ

ABSTRACT

We analyze the physical conditions, chemical composition and other properties of the photoionized Herbig-Haro object HH 204 – as well as the Diffuse Blue Layer and the neighboring area of the Orion Nebula – through Very Large Telescope (VLT) echelle spectroscopy and Hubble Space Telescope (*HST*) imaging. We study the sub-arcsecond distribution of physical conditions and ionic abundances of HH 204. We find an abrupt increase of $T_e(\text{[O III]})$ in the bowshock, showing that the high ionization degree gas – that represents $\lesssim 1\%$ of the total gas – is affected by shock heating while the rest seems to be in photoionization equilibrium. We estimate the $t^2(\text{O}^{2+})$ representative of the entire volume of HH 204, the first plausible direct determination of this parameter in a nebular object. For each gas component, we derive the ionic abundances of O^+ , O^{2+} , N^+ , Ne^{2+} , S^+ , S^{2+} , Cl^+ , Cl^{2+} , Ar^{2+} , Ar^{3+} , Fe^+ , Fe^{2+} , Fe^{3+} , Ni^+ , Ni^{2+} , Ca^+ and Cr^+ based on collisionally excited lines (CELs) and those of He^+ , O^+ , O^{2+} and C^{2+} based on recombination lines (RLs). In HH 204, the O^+ abundance determined from CELs matches the one based on RLs. Since $\text{O} \approx \text{O}^+$ in HH 204, we can say that the abundance discrepancy is zero for this element. In HH 204, we find that the ionic abundances of Ni and Fe have similar ionization and depletion patterns. The total abundances of these elements are a factor of 3.5 higher than in the rest of the Orion Nebula due to dust destruction in the bowshock. We derive the chemical composition of the Diffuse Blue Layer by the first time. By adding the emission of all the kinematical components – simulating a lower spectral and spatial resolution spectrum –, we show that the analysis of a single spectrum containing components with different physical conditions can lead to wrong determinations of chemical abundances, mainly due to incorrect estimations of the electron density.

Keywords: ISM:Abundances – ISM: Herbig–Haro objects – ISM: individual: Orion Nebula – ISM: individual: HH 204 – ISM: individual: Diffuse Blue Layer

1. INTRODUCTION

HH 204 is a Herbig-Haro (HH) object located in the central region of the Orion Nebula, just southeast of the

Orion Bar, apparently close to the θ^2 Ori A star. It was observed by Münch & Wilson (1962) and classified as an HH by Cantó et al. (1980). The origin of the jet is usually associated with the Orion South molecular cloud (Orion-S) (O'Dell et al. 2017a), an active star formation area of the Orion Nebula. However, the source of the driving jets that feed HH 204 is not entirely clear as we discuss in this paper. HH 204 is photoionized

Corresponding author: José E. Méndez-Delgado
jemd@iac.es

by θ^1 Ori C from behind its direction of propagation, through the cavity formed by the shock (O'Dell et al. 1997a, 2017a). There are several works where this object and the neighboring HH 203 have been studied (Doi et al. 2004; Henney et al. 2007; García-Díaz et al. 2008; O'Dell et al. 2015, and references therein), investigating their proper motions, structure and kinematics of the zone of the Orion Nebula where the shock takes place. Through long-slit spectra, Mesa-Delgado et al. (2008) studied the effects of HH 204 on the gas of the Orion Nebula, finding peaks in the density and temperature distributions when crossing its surrounding area as well as increases in the emission flux of [Fe III] lines produced by dust destruction. Using integral field spectroscopy, Núñez-Díaz et al. (2012) studied the influence of HH 204 in the Orion Nebula in an area 16×16 arcsec 2 , finding the presence of a trapped ionization front as well as arguments in favor of the location of the object within the main body of the Orion Nebula and not in the Veil. The works by Mesa-Delgado et al. (2008), Núñez-Díaz et al. (2012) and O'Dell et al. (2017a) show the presence of a high- T_e ([N II]) zone, attributed to shock heating. However, this effect and the coincidental fall in the total abundance of O, may be related with an underestimation of n_e , an alternative explanation that will be discussed in Sec. 7.

This is the second article in a series dedicated to study photoionized HH objects in the Orion Nebula using high-resolution spectroscopy obtained with the Ultraviolet and Visual Echelle Spectrograph (UVES) (D'Odorico et al. 2000) of the Very Large Telescope (VLT) and the *Hubble Space Telescope* (*HST*) imaging. In this work, we analyze the physical conditions, chemical composition and dynamical properties of HH 204, separating the emission of the Orion Nebula from the HH object and other ionized gas components present in the line of sight. Previous to the present paper, there are few works dedicated to high-resolution spectroscopy of photoionized HH objects of the Orion Nebula, as HH 202 S (Méndez-Delgado et al. 2009), HH 529 II and HH 529 III (Blagrave et al. 2006; Méndez-Delgado et al. 2021).

This paper has the following content: in Sec. 2 we describe the observational data and its treatment. In Sec. 3 we describe the measurement of the spectral lines and the reddening correction. In Sec. 4 we derive the physical conditions and the ionic abundances of each of the observed velocity components, while in Sec. 5 we focus exclusively on HH 204, deriving their physical conditions, ionic abundances and some properties pixel-by-pixel along the UVES slit, as well as study the spatial distribution of the emission of HH 204 with *HST* imaging. In Sec. 6 we estimate the total abundances of the

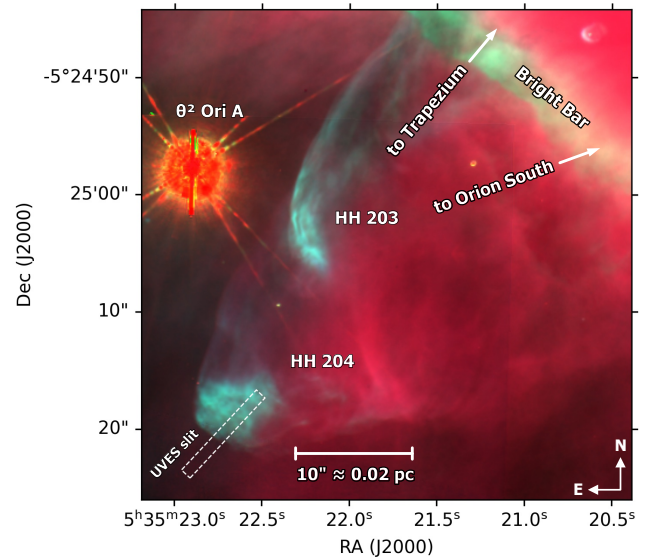


Figure 1: Location of the UVES spectrograph slit at the head of the HH 204 bow shock. The background RGB images shows the immediate environs of HH 203 and 204, derived from *HST* WFPC2 observations (O'Dell & Wong 1996) in filters of [O III] (red), [N II] (green), and H α (blue) .

observed gas components. In Sec. 7 we study the effects of mixing three gas components of very different density along the line of sight, simulating a spectrum with lower spectral resolution. In Sec. 8, we investigate the origin of HH 204 and its relation with HH 203. In Sec. 9 we discuss the main results of this work and their implications. Finally, in Sec. 10 we summarize the conclusions. In the Appendix A we show the reliability of the [Fe III] atomic data that we use. In Appendix B tables of data and figures are added as support material.

2. OBSERVATIONS AND DATA REDUCTION

The observations were made during the nights of October 28 and 29, 2013 under photometric conditions using UVES in the UT2 of the Very Large Telescope (VLT) in Cerro Paranal, Chile. The slit position was centred at the coordinates RA(J2000)= $05^h35^m22^s.72$, DEC(J2000)= $-05^\circ25'20.42''$ with a position angle of 137° . The slit width provides an effective spectral resolution $\lambda/\Delta\lambda \approx 6.5$ km s $^{-1}$, covering the spectral range between 3100–10420Å. Three exposures of 150s of the standard star GD71 (Moehler et al. 2014a,b) were taken in the same night under similar observational conditions than the science images to achieve the flux calibration of the data. The observational settings are shown in Table 1 and the spatial coverage is presented in Fig. 1.

Table 1: Main parameters of UVES spectroscopic observations.

Date	$\Delta\lambda$ (Å)	Exp. time (s)	Seeing (arcsec)	Airmass
2013-10-29	3100-3885	5, 3×180	0.85	1.10
2013-10-29	3750-4995	5, 3×600	0.70	1.16
2013-10-29	4785-6805	5, 3×180	0.85	1.10
2013-10-29	6700-10420	5, 3×600	0.70	1.16

The instrumental configuration and the data reduction procedure is described in Méndez-Delgado et al. (2021, hereinafter Paper I). The 2D spectra (see Fig. 2) shows three evident components: the nebular one (the emission of the Orion Nebula), which is rather homogeneously distributed along the spatial axis of the slit and occupies the reddest spectral position; the “Diffuse Blue Layer”, (hereinafter DBL) a slightly blueshifted homogeneous diffuse component, previously detected by Deharveng (1973) that may correspond to a different H II region along the same line of sight (García-Díaz & Henney 2007) and HH 204, the “ball-shaped” blueshifted component. We define two spatial cuts – shown in Fig. 2 – covering a spatial area of 7.38 arcsec for cut 1 and 1.97 arcsec for cut 2. In cut 2, we can separate the emission of the DBL and the nebular component. However, due to the strong contribution of HH 204, we can not separate those components in cut 1. In this case, we study the emission of the combined spectrum of the nebular component and the DBL. We also take advantage of the quality of the data performing a pixel-by-pixel analysis of various emission lines in order to detect small variations in physical conditions and/or the chemical composition of HH 204 along the slit.

The study of the spatial distribution of the emission of HH 204 and the gas flows that may originate it are based in the *HST* WFC2 imaging in the F502N, F547M, F656N, and F658N filters from program GO5469 (O’Dell & Wong 1996). The spatial pixel size of these data is 0.045 arcsec. Flux calibration and correction for contamination by continuum and non-target lines was performed using the coefficients given in O’Dell (2009).

3. LINE INTENSITIES AND REDDENING

Table 2: Reddening coefficients for each component.

c(H β)		
	HH 204	Nebula + DBL
Cut 1	0.42 ± 0.02	0.31 ± 0.03
DBL		Nebula
Cut 2	0.42 ± 0.09	0.30 ± 0.04

We use SPLIT task from IRAF¹ (Tody 1993) to measure the line intensities and estimate their uncertainties as it is described in detail in Paper I. In the case of the spectra of cut 1 and cut 2, we measure a complete set of around ~ 500 and ~ 300 emission lines, respectively, while in the case of the pixel-by-pixel measurements for HH 204, we limit the analysis to some representative lines: H9, H β , H α ; HeI $\lambda\lambda\lambda 4471, 5876, 6678$; [N II] $\lambda\lambda 5755, 6584$; O I $\lambda 7772$; [O I] $\lambda 6300$; [O II] $\lambda 3726$; [O III] $\lambda\lambda 4363, 4959$; [Ne III] $\lambda 3869$; [S II] $\lambda\lambda 6716, 6731$; [S III] $\lambda\lambda 6312, 9531$; [Cl II] $\lambda 9124$; [Cl III] $\lambda 5538$; [Ar III] $\lambda 7136$; [Ca II] $\lambda 7324$; [Cr II] $\lambda 8000$; [Fe II] $\lambda 9052$; [Fe III] $\lambda\lambda 4658, 4702, 4881$; [Ni II] $\lambda 7378$ and [Ni III] $\lambda 7890$. The reddening correction was done using the extinction curve from Blagrave et al. (2007) and the emissivity coefficients of Storey & Hummer (1995) for H ϵ , H δ , H γ , H β and H α Balmer lines and the P12, P11, P10, P9 Paschen lines. The values of the extinction coefficient, $c(H\beta)$, are presented in Table 2. In the case of pixel-by-pixel measurements, a value of $c(H\beta) = 0.42 \pm 0.02$ was used. An example of the spectra that can be found in the online material is shown in Table 9, where some lines of the spectra of cut 1 are shown.

4. ANALYSIS OF INTEGRATED SPECTRA OF EACH COMPONENT

4.1. Physical Conditions

We use the version 1.1.13 of PyNeb (Luridiana et al. 2015) to obtain the physical conditions of the gas from the intensity ratios of collisionally excited lines (CELs) and recombination lines (RLs). PyNeb is a Python based tool to compute line emissivities and derive physical conditions and chemical abundances of ionized gas. We have used the atomic data set presented in tables 10 and 11 for the calculations made with PyNeb. We first

¹ IRAF is distributed by National Optical Astronomy Observatory, which is operated by Association of Universities for Research in Astronomy, under cooperative agreement with the National Science Foundation

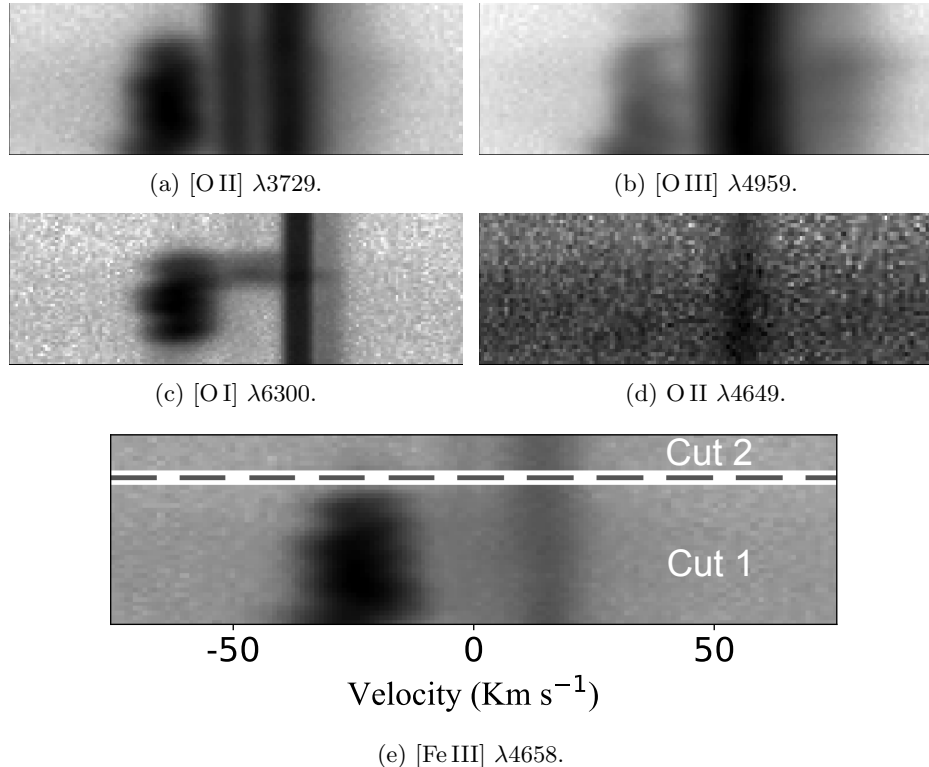


Figure 2: *Upper panels:* Sample of representative lines in the bi-dimensional spectrum. The Y axis corresponds to the spatial direction (up southeast, down northwest, see Fig. 1 for the spatial location of the slit) while the X axis is the spectral axis. All figures are centered at λ_0 , the rest-frame reference wavelength of each line. The “ball-shaped” emission corresponds to HH 204. The slightly blue shifted component with respect to the nebular one is the “Diffuse Blue Layer” (Deharveng 1973; García-Díaz & Henney 2007), mainly noticeable in the emission of low ionization ions such as [O II]. *Bottom panel:* Emission of the [Fe III] $\lambda\lambda 4658$ line as well as the limits and extension of the different spatial cuts selected to analyse each velocity component. Cut 1 is at the bottom, which corresponds to the westernmost one. The spatial coverage is 7.38 arcsec and 1.97 arcsec for cuts 1 and 2, respectively. The velocity scale is heliocentric.

estimate the electron density, n_e , given by each diagnostic of CELs by calculating each convergence of $T_e - n_e$ with the available diagnostics of electron temperature, T_e , using the PyNeb task *getCrossTemDen*, as it is described in detail in Paper I. Then, in the nebular and DBL components, we adopt the weighted mean² of the available values of n_e obtained with the following diagnostics: [O II] $\lambda 3726/\lambda 3729$, [S II] $\lambda 6731/\lambda 6716$ and [Cl III] $\lambda 5538/\lambda 5518$. For consistency, in the case of HH 204 we rely on the n_e derived from [Fe III] lines since values of $10^4 - 10^6 \text{ cm}^{-3}$, are above the critical densities of the CELs involved in the more common diagnostics. The simultaneous estimation of n_e ([Fe III]) and T_e ([Fe III]) in HH 204 is achieved by a maximum-likelihood procedure, as described in Paper I. However, in HH 204, we have confident detections of [Fe III]

$\lambda\lambda 3240, 3335$ lines from the ${}^5\text{D} - {}^3\text{D}$ transitions, which arise from higher levels than multiplets ${}^5\text{D} - {}^3\text{F}$ and ${}^5\text{D} - {}^3\text{P}$ that give origin to some of the strongest [Fe III] lines such as, for example, $\lambda\lambda 4658, 4702, 4734$ and $\lambda\lambda 4930, 5271, 5011$, respectively. Thus, the ratios of the lines coming from the aforementioned multiplets are highly dependent on T_e as it is shown in Fig. 3. We include the following lines in the maximum-likelihood calculation: [Fe III] $\lambda\lambda 3240, 3335, 4658, 4702, 4734, 4881, 5011, 5271$. This collection of lines allows us to obtain well-constrained values of T_e ([Fe III]) and n_e ([Fe III]). The intensity ratios of these selected lines are consistent with the predicted ones when using transitions coming from the same atomic level (which are independent of the physical conditions of the gas), as we show in Table 12. Another density indicator that can be derived from our data is n_e (O II), but only for the nebular component, which is the only one where we detect RLs of multiplet 1 of O II.

² The weights were defined as the inverse of the square of the error associated to each density diagnostic.

Once the representative n_e is adopted for each component, we estimate T_e through several diagnostics based on CELs as it is shown in Table 3. In the case of $T_e(\text{[S III]})$, telluric absorptions affect the line $\lambda 9069$ in the nebular and DBL components. Thus, we adopt $I(\text{[S III]} 9531)/I(\text{[S III]} 9069) = 2.47$ (Podobedova et al. 2009) in these cases. In HH 204 we were able to separate the auroral [O I] $\lambda 5577$ line from sky emission contamination, which permitted us to estimate $T_e(\text{[O I]})$. In the DBL, the estimations of $T_e(\text{[O II]})$ and $T_e(\text{[S II]})$ are affected by some extended residual emission of HH 204 in the auroral lines that crosses the cut border, affecting the first pixels of cut 2. $T_e(\text{He I})$ was estimated using the average values obtained from $I(\lambda 7281)/I(\lambda 6678)$, $I(\lambda 7281)/I(\lambda 4922)$ and $I(\lambda 7281)/I(\lambda 4388)$ He I line intensity ratios. Finally, we define $T_e(\text{low})$ as the weighted mean of $T_e(\text{[N II]})$, $T_e(\text{[O II]})$ and $T_e(\text{[S II]})$ while $T_e(\text{high})$ is the weighted mean of $T_e(\text{[O III]})$ and $T_e(\text{[S III]})$.

The resulting physical conditions for all components are shown in Table 3.

4.2. Ionic abundances

We assume the values of the n_e and T_e indicator appropriated for each ion –assuming a three-zone approximation– to derive the ionic abundances of the different components. We use $T_e(\text{low})$ for N^+ , O^+ , S^+ , Cl^+ , Ca^{2+} , Cr^+ , Fe^+ , Fe^{2+} , Ni^+ and Ni^{2+} and $T_e(\text{[S III]})$ for S^{2+} and Cl^{2+} . In the case of Ne^{2+} , O^{2+} and Ar^{3+} , we use $T_e(\text{high})$. We use $T_e(\text{high})$ to derive the He^+ , C^{2+} and Ar^{2+} abundances for the nebular component, but $T_e(\text{low})$ for HH 204, as we discuss in Sec. 5.1. We follow the same methodology described in Paper I for abundance calculations, except in some particular cases that are discussed below together with some ionic abundance determinations not considered in Paper I.

4.3. Ionic abundances of Fe and Ni ions

In HH 204, the emission lines of [Fe II], [Ni II], [Fe III] and [Ni III] are considerably enhanced in comparison with what is observed in the nebular component. We were able to observe weak lines of multiplets and transitions from these ions which allows us to explore their abundances in detail. Optical lines coming from the upper levels of the Fe^+ atom can be affected by continuum pumping (Lucy 1995; Rodríguez 1999; Verner et al. 2000). However, lower levels that produce the emission lines of multiplet $a^4F - a^4P$ are mostly populated by collisions (Baldwin et al. 1996). One of the strongest lines of this multiplet, [Fe II] $\lambda 8617$ ($a^4F_{9/2} - a^4P_{5/2}$), could not be detected due to the instrumental gap of UVES in the red arm. However, weaker lines arising

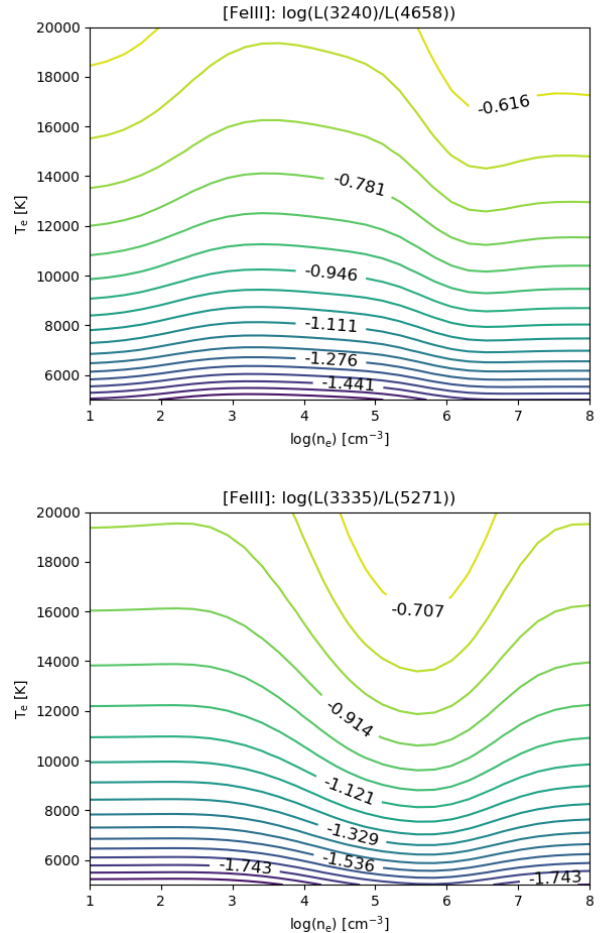


Figure 3: Predicted dependence of the [Fe III] $\lambda 3240/\lambda 4658$ and $\lambda 3335/\lambda 5271$ line intensity ratios with physical conditions.

from the same upper level as $\lambda\lambda 9052, 9399$ ($a^4F_{7/2} - a^4P_{5/2}, a^4F_{5/2} - a^4P_{5/2}$), detected in HH 204, must be useful for the same purpose. Although the transition probabilities of the weakest detected lines coming from the $a^4P_{1/2}$, $a^4P_{3/2}$ and $a^4P_{5/2}$ levels should be revised (in addition to possible undetected telluric absorptions), there is a good agreement between the measured and predicted line ratios of [Fe II] 9052/9399, 8892/9227 and 9268/9034, as it is shown in Table 13. In order to make a simple test of the chosen atomic data, we take advantage of the theoretical density dependence between the population of the $a^4P_{1/2}$ and the $a^4P_{5/2}$ levels as it is shown in Fig. 4. By using the estimated $T_e(\text{low})$ for HH 204 and the [Fe II] $\lambda 9268/\lambda 9052$ intensity ratio, we obtain $n_e(\text{[Fe II]}) = 13100^{+2860}_{-2990} \text{ cm}^{-3}$, which is consistent with the rest of density diagnostics shown in Table 3. In the Nebula+DBL spectra from cut 1, [Fe II] lines are partially enhanced by the strong emission of

Table 3: Physical conditions determined from several diagnostics.

Diagnostic	Cut 1		Cut 2	
	HH 204	Nebula + DBL	DBL	Nebula
n_e (cm $^{-3}$)				
[O II] $\lambda\lambda 3726/\lambda 3729$	15420 $^{+7740}_{-3850}$	1130 $^{+150}_{-110}$	400 $^{+140}_{-120}$	1480 $^{+190}_{-180}$
[S II] $\lambda\lambda 6731/\lambda 6716$	11350 $^{+9920}_{-3890}$	1350 $^{+290}_{-260}$	300 $^{+140}_{-120}$	1230 $^{+250}_{-230}$
[Cl III] $\lambda\lambda 5538/\lambda 5518$	13370 $^{+1990}_{-1830}$	1630 $^{+370}_{-320}$	-	1930 $^{+720}_{-650}$
[Fe II] $\lambda\lambda 9268/\lambda 9052$	13100 $^{+2860}_{-2990}$	-	-	
[Fe III] $\lambda\lambda 4658/\lambda 4702$	13040 $^{+3830}_{-3130}$	3380 $^{+1810}_{-1340}$	-	3200 $^{+2540}_{-1540}$
n_e (O II)	-	1350 \pm 150	-	1050 \pm 200
[Fe III] [*]	13540 \pm 1210	-	-	-
Adopted	13540 \pm 1210	1230 \pm 160	350 \pm 50	1440 \pm 170
T_e (K)				
T_e (He I)	8790 $^{+480}_{-430}$	9760:	5650:	7980:
[O I] $\lambda\lambda 5577/\lambda\lambda 6300+64$	8290 $^{+430}_{-320}$	-	-	-
[N II] $\lambda\lambda 5755/\lambda 6584$	8760 $^{+170}_{-180}$	8530 $^{+150}_{-190}$	8120 $^{+390}_{-360}$	8440 $^{+170}_{-210}$
[O II] $\lambda\lambda 3726+29/\lambda\lambda 7319+20+30+31$	-	-	10390 $^{+730}_{-640}$	9120 $^{+430}_{-470}$
[S II] $\lambda\lambda 4069+76/\lambda\lambda 6716+31$	8260 $^{+640}_{-500}$	11470 $^{+950}_{-630}$	10440 $^{+1360}_{-1030}$	9890 $^{+650}_{-610}$
[O III] $\lambda\lambda 4363/\lambda\lambda 4959+5007$	12430 $^{+180}_{-220}$	8010 $^{+90}_{-80}$	-	8120 $^{+90}_{-100}$
[S III] $\lambda\lambda 6312/\lambda\lambda 9069+9531$	9310 $^{+220}_{-330}$	8180 $^{+190}_{-230}$	7710 $^{+510}_{-400}$	8010 $^{+250}_{-210}$
[Fe III] [*]	8210 \pm 220	-	-	-
T_e (low) Adopted	8760 \pm 180	8530 \pm 190	8120 \pm 390	8440 \pm 210
T_e (high) Adopted	12430 \pm 220	8030 \pm 60	7710 \pm 510	8110 \pm 90

NOTE—* indicates that a maximum likelihood method was used.

HH 204. Since the [Fe II] lines in that combined component are rather weak, any small contribution from the tail of the HH 204 emission can significantly affect the Fe $^+$ abundance. This is not a problem in cut 2, where the Fe $^+$ abundance of the nebular component can be derived from the uncontaminated [Fe II] $\lambda 8892$ line.

Due to the low ionization degree of HH 204, we expect that Fe $^+$ and Ni $^+$ have an important contribution to the total Fe and Ni abundances. Therefore, it seems pertinent to discuss in some detail the degree of confidence of the abundance determinations based on these two ions. The a 4 F – a 4 P $_{5/2}$ transitions of [Fe II] and the a 2 D – a 2 F $_{7/2}$ ones of [Ni II] have practically the same excitation energy, giving origin to lines close in wavelength (Bautista et al. 1996). However, there is an important difference between their sensitivity to fluorescence by continuum pumping due to the multiplicity of their ground states. Photoexcitations from the Fe $^+$ 6 D ground state to the quartet levels have low probability and lines produced by intercombination transitions from sextet to quartet levels should be very weak (Bautista & Pradhan 1998). However, Rodríguez (1999) pointed out that the lowest quartet level, a 4 F $_{9/2}$, may be metastable

and promote excitations to higher quartet levels. The main pumping routes starting in this level were studied by Verner et al. (2000) at densities above 10 4 cm $^{-3}$, finding that this pumping populates the levels a 4 H, b 4 F, b 4 P and a 4 G. Since transitions from any of these levels to a 4 P are rather weak, its population remains practically unaffected. Nevertheless, in the case of [Ni II], the ground state and the participating levels are doublets which make fluorescence effects by continuum pumping more likely (Bautista et al. 1996). However, an important factor that plays against the influence of fluorescence effects in [Ni II] in the case of HH 204 is its relatively large distance from θ^1 Ori C (150.4 arcsec), the main ionization source of the nebula (O'Dell et al. 2015, 2017b). In a simple procedure, following the formalism developed by Bautista et al. (1996, their equation 8), for a 3-level model (level 1: a 2 D $_{5/2}$, level 2: a 2 F $_{7/2}$ and level 3: z 2 D $_{5/2}^0$), the critical densities n_{cf} – for which if $n_e > n_{cf}$, collisional excitations dominate over fluorescence – in two zones of the Orion Nebula (a and b), both excited by θ^1 Ori C, should be related as follows:

$$\frac{n_{cf, a}}{n_{cf, b}} = \left(\frac{J_{13, a}}{J_{13, b}} \right) \left(\frac{q_{12, b}}{q_{12, a}} \right), \quad (1)$$

where q_{12} is the Maxwellian averaged collisional strength for transitions from level 1 to 2 and J_{13} is the intensity of the continuum at energies of the $1 \rightarrow 3$ transitions. If we choose the zone “a” as the one observed by Osterbrock et al. (1992) and the zone “b” as HH 204, we can assume $q_{12, b}/q_{12, a} \approx 1$, because the T_e determined by Osterbrock et al. (1992) and us are very similar (9000 K and 8760 K, respectively). On the other hand, by estimating the geometrical dilution of J_{13} in both areas (the zone observed by Osterbrock et al. (1992) is located at 63.98 arcsecs from θ^1 Ori C), we get a $n_{\text{cf}, a}/n_{\text{cf}, b} \approx 5.53$. By adopting the $n_{\text{cf}, a}$ estimated by Bautista et al. (1996), we obtain $n_{\text{cf}, b} \approx 2.17 \times 10^3 \text{ cm}^{-3}$, which is rather small compared with the density we obtain for HH 204 and therefore collisional excitation should dominate. Nevertheless, it must be considered that the apparently closer star θ^2 Ori A may be also a source of fluorescence for HH 204. However, by using the [Ni II] $\lambda 7378$ ($a^2D_{5/2} - a^2F_{7/2}$) line to obtain the Ni^+ abundance and comparing with the Fe^+/H^+ ratio, we obtain $\log(\text{Ni}^+/\text{Fe}^+) = -1.27 \pm 0.06$, which is in complete agreement with the solar value of $\log(\text{Ni}/\text{Fe})_\odot = -1.25 \pm 0.05$ (Lodders 2019), suggesting the absence of significant fluorescence effects (we expect larger fluorescence effects in Ni^+). Therefore, we can assume that θ^2 Ori A is not a significant source of photon pumping of [Ni II] lines in HH 204. Since some [Ni II] lines, as $\lambda 7412$ ($^2D_{3/2} - ^2F_{5/2}$), give Ni^+ abundances around a factor 2.20 higher than others, continuum pumping effects should be still important in the higher levels of the Ni^+ atom in HH 204, although in a much lesser extent than in the area of the Orion Nebula observed by Osterbrock et al. (1992), where this factor reaches a value of 15.51 (Lucy 1995). We do not estimate the Ni^+ abundances for the rest of velocity components because it requires a detailed analysis of the fluorescence conditions in the ionized gas, which goes beyond the scope of this paper.

We derive the Fe^{2+} abundance using the [Fe III] lines indicated in Sec. 4.1. It is noticeable the good agreement between $T_e([\text{Fe III}])$, $T_e([\text{O I}])$ and $T_e([\text{S II}])$ in the case of HH 204, contrary to what was found in HH 529 II and HH 529 III, where $T_e([\text{Fe III}])$ was more consistent with the temperature obtained for high ionization ions (Méndez-Delgado et al. 2021). This is not surprising due to the different ionization degrees of HH 204 and HH 529 II+III (see Sec. 5).

In Paper I, we pointed out the inconsistency between the predicted and measured intensity ratios of [Ni III] $^3F - ^3P_2$ transitions ($\lambda\lambda 6534, 6000, 6946$) in HH 529 II, HH 529 III, HH 202 S and several zones of the Orion Nebula (see Table D11 of Paper I). We obtain a similar

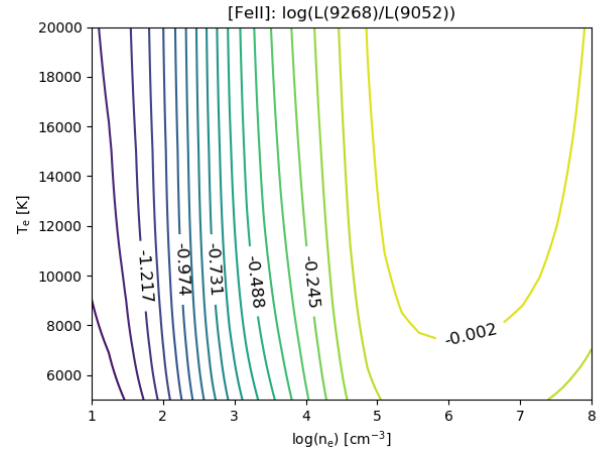


Figure 4: Predicted dependence of the [Fe II] $\lambda 9268/\lambda 9052$ line intensity ratios with physical conditions.

result for HH204, $\lambda 6534/\lambda 6000 = 1.38 \pm 0.18$, which is rather far from the predicted value of 2.19 value (Bautista 2001). We have a different situation for the intensity ratios of lines arising from the 1D_2 level. After subtracting the small contribution of [Cl III] $\lambda 8499.60$ to the measured intensity of [Ni III] $\lambda 8499.62$, we obtain [Ni III] $\lambda 7890/\lambda 8500 = 2.65 \pm 0.19$ in agreement with the predicted value of 2.47 (Bautista 2001). This indicates that, with the available atomic data, the most confident determinations of the Ni^{2+} abundance can be obtained with these last lines. Thus, we will adopt the Ni^{2+} abundances determined from [Ni III] $\lambda 7890$ line. Unfortunately, this line is affected by a telluric emission feature in the nebular component and, therefore, we have to rely on the [Ni III] $\lambda 6534$ line to determine the Ni^{2+} abundance for this component.

4.4. Ionic abundances of Ca^+ and Cr^+

We measure some [Ca II] and [Cr II] lines with a good signal-to-noise ratio in HH 204. Thus, it permits us to estimate Ca^+ and Cr^+ abundances. However, [Cr II] lines may be affected by fluorescence similarly to [Ni II] ones. The energies corresponding to $a^2D - a^2F_{7/2}$ transitions of [Ni II] are similar to $a^6S - a^6D$ ones of [Cr II]. Moreover, in both cases the lower – ground – and upper levels have the same multiplicity, so the excitation of the upper level by starlight is likely. Therefore, it seems reasonable to assume that if fluorescence effects are important for [Ni II] lines, they will also be important for [Cr II] lines. As we discuss in Sec. 4.3, in HH 204 collisional excitations dominate over fluorescence in the aforementioned [Ni II] transitions and this may be also the case for [Cr II]. With this assumption,

tion, we obtain an abundance of $12 + \log(\text{Cr}^+/\text{H}^+) = 4.28 \pm 0.03$. By comparing this value with the Fe^+ and Ni^+ abundances, we obtain $\log(\text{Cr}^+/\text{Ni}^+) = -0.61 \pm 0.05$ and $\log(\text{Cr}^+/\text{Fe}^+) = -1.88 \pm 0.07$, in agreement with the solar values of $\log(\text{Cr}/\text{Ni})_\odot = -0.57 \pm 0.05$ and $\log(\text{Cr}/\text{Fe})_\odot = -1.82 \pm 0.04$, respectively (Lodders 2019). Nevertheless, the spatial distribution of the Cr^+/Ni^+ and Cr^+/Fe^+ ratios along the HH 204 jet is not completely constant, as it is described in Sec. 5.2, which may be indicative of different ionization/depletion patterns between these elements. Unfortunately, although several [Cr III] lines are detected, we can not derive the Cr^{2+} abundance due to the lack of atomic data for this ion.

In the case of the Ca^+ abundance, we base our estimations in the [Ca II] $\lambda 7324$ line since $\lambda 7291$ is affected by a telluric absorption in our observations. Due to its low ionization potential, smaller than that of hydrogen, and owing to the presence of an ionization front in HH 204 (Núñez-Díaz et al. 2012), the resulting abundance may not represent the real gaseous Ca^+ abundance in the photoionized gas of HH 204.

4.5. Ionic abundances based on RLs

For the nebular component, the He^+ abundance is derived using $T_e(\text{high})$ and the lines considered in Table D14 of Paper I, which are the least affected by the metastability of the 2^3S level. However, we have used $T_e(\text{low})$ for HH 204. In this component, our determination of $T_e(\text{He I})$ is more consistent with $T_e(\text{low})$. This is because in HH 204, [O III] emission arises from a small localized area of higher ionized gas and $T_e([\text{O III}])$ may be not representative of the He^+ volume, as we describe in Sec. 5.1.

$\text{C II } \lambda 4267$ is partially blended in the two velocity components of cut 1 and therefore we base our calculations on $\text{C II } \lambda 9903$. We use $\text{C II } \lambda 4267$ in cut 2. C^{2+} abundance estimations based on both lines are in complete agreement in cut 2. Due to the similar ionization potentials of C^+ and He^0 and the considerations outlined in the previous paragraph, $T_e(\text{low})$ is also used for determining the C^{2+} abundance in HH 204.

Contrary to the situation presented in Paper I, in HH 204, O I RLs from multiplet 1 are severely affected by telluric emission features with the exception of O I $\lambda 7772$. We derive the O^+ abundance of the HH object using the intensity of this line and the predicted line strengths from Wiese et al. (1996) following Eq. 2 of Esteban et al. (1998).

Estimations of the O^{2+} abundance from RLs are based on the available O II lines of multiplet 1. These are not detected in the case of HH 204 (see Fig. 5). We use an

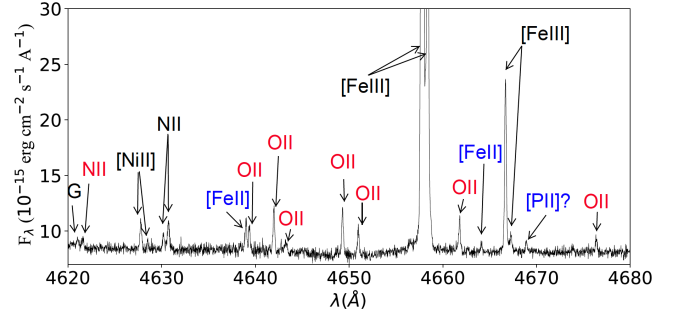


Figure 5: Section of the spectrum of the spatial cut 1 covering the spectral range 4620–4680 Å. Lines emitted exclusively by HH 204 are marked in blue, while those of the Orion Nebula are marked in red. The lines observed in both components are highlighted in black. Several O II RLs from multiplet 1 are present in the nebular component, but they are not observed in HH 204 due to its low ionization potential. The emission marked with a G is a ghost feature.

estimate of the upper limit of the intensity of $\lambda 4649$ line for this component.

5. UNVEILING HH 204

As it was mentioned in Sec. 3 we measure several lines pixel by pixel throughout the spatial coverage of HH 204. The spatial resolution in the blue and red arms of UVES is slightly different ($0.246''/\text{pixel}$ and $0.182''/\text{pixel}$ respectively). Cut 1 include 30 pixels in the blue arm and 42 in the red one. In the pixel by pixel measurements, renormalization between lines in common in each arm is not enough to dilute possible differences in the integrated flux. However, $\text{H}\beta$ is observed in the spectra of both arms and therefore we split our pixel-spectra in two parts, 27 blue-pixel-spectra and 37 red-pixel-spectra, both groups normalized with respect to $f(\text{H}\beta)$. The missing first pixels (from east to west) of cut 1 of both arms were not included since the emission of HH 204 was too faint. We proceeded as follows: based on the $[\text{Fe III}] \lambda 4658/\lambda 4702$ line ratios we derive n_e along HH 204 in the blue arm. Once the density distribution was estimated, the calculation of $T_e([\text{O III}])$ was done, also in the blue arm through the $[\text{O III}] \lambda 4363/\lambda 4959$ line ratio. The spatial distribution of n_e was linearly interpolated in the red arm to estimate $T_e([\text{S III}])$ and $T_e([\text{N II}])$. Once the physical conditions are determined, we estimate the ionic abundances using the same procedure followed in Sec. 4.2. The zero point of the spatial distribution is located at coordinates: RA(J2000)= $05^{\text{h}}35^{\text{m}}22^{\text{s}}.81$, DEC(J2000)= $-05^{\circ}25'21.86''$, just at the apparent eastern – external – edge of the bowshock. To estimate the distance from the bowshock along the jet, we adopt an

Table 4: Chemical abundances obtained with CEL's of the integrated spectra of each component.

Ion	Cut 1		Cut 2	
	HH 204	Nebula + DBL	DBL	Nebula
O ⁺	8.62 ± 0.05	8.14 ± 0.05	8.26 ^{+0.13} _{-0.09}	8.18 ^{+0.06} _{-0.05}
O ²⁺	6.34 ± 0.02	7.96 ± 0.02	7.33 ^{+0.15} _{-0.10}	8.04 ± 0.02
N ⁺	7.72 ± 0.03	7.34 ± 0.03	7.40 ^{+0.08} _{-0.06}	7.29 ^{+0.04} _{-0.03}
Ne ²⁺	5.05 ± 0.03	7.16 ± 0.02	-	7.23 ^{+0.03} _{-0.02}
S ⁺	6.60 ± 0.04	5.93 ± 0.03	5.92 ^{+0.07} _{-0.06}	5.86 ^{+0.04} _{-0.03}
S ²⁺	6.80 ± 0.03	6.84 ± 0.03	6.85 ^{+0.10} _{-0.08}	6.89 ± 0.04
Cl ⁺	4.72 ± 0.03	4.17 ± 0.03	4.08 ^{+0.10} _{-0.09}	4.05 ± 0.04
Cl ²⁺	4.77 ^{+0.04} _{-0.03}	4.93 ± 0.04	4.99 ^{+0.16} _{-0.12}	4.98 ^{+0.06} _{-0.05}
Ar ²⁺	5.66 ± 0.03	6.10 ± 0.02	5.99 ^{+0.10} _{-0.08}	6.12 ± 0.02
Ar ³⁺	-	3.64 ^{+0.13} _{-0.12}	-	-
Fe ⁺	6.16 ± 0.04	-	-	4.72 ± 0.08
Fe ²⁺	6.49 ± 0.02	5.72 ± 0.04	5.56 ^{+0.10} _{-0.08}	5.77 ± 0.04
Fe ³⁺	< 5.11	5.73 ± 0.13	-	-
Ni ⁺	4.89 ± 0.02	-	-	-
Ni ²⁺	5.13 ± 0.03	4.37 ± 0.09	-	-
Ca ⁺	3.50 ± 0.03	-	-	-
Cr ⁺	4.28 ± 0.03	-	-	-

NOTE—Abundances in units of 12+log(Xⁿ⁺/H⁺).**Table 5:** Chemical abundances obtained with RL's of the integrated spectra of each component.

Ion	Cut 1		Cut 2	
	HH 204	Nebula + DBL	DBL	Nebula
He ⁺	10.53 ± 0.02	10.85 ± 0.03	10.66 ± 0.06	10.92 ± 0.04
O ⁺	8.57 ± 0.03	-	-	-
O ²⁺	< 7.54	8.25 ± 0.06	-	8.40 ± 0.03
C ²⁺	7.76 ± 0.07	8.22 ± 0.04	-	8.37 ± 0.02

NOTE—Abundances in units of 12+log(Xⁿ⁺/H⁺).

heliocentric distance of 410 ± 10 pc (Binder & Povich 2018) to the Orion Nebula, based on *Gaia* DR2 parallaxes (Gaia Collaboration et al. 2018).

5.1. Small scale physical conditions

The resulting pixel by pixel distribution of physical conditions is shown in Fig. 6. We can see that n_e ([Fe III]) increases as one approaches the shock front up to a factor of about 2, compared to the values at \sim 13 mpc from the bowshock. The distribution of T_e ([N II]) is practically constant, while T_e ([S III]) decreases slightly as

we approach the edge of the bowshock. Conversely, T_e ([O III]) strongly increases when one approaches the bowshock.

The interpretation of the spatial distribution of T_e ([O III]) is complex. In the presence of a shock, a photoionized gas can be heated at a temperature higher than that fixed by photoionization equilibrium (Zel'dovich & Raizer 1967) (see Sec. 11 of Paper I). After the shock passage, the gas cools down by radiative emission until reaching equilibrium temperature, forming a cooling zone whose extension will be inversely pro-

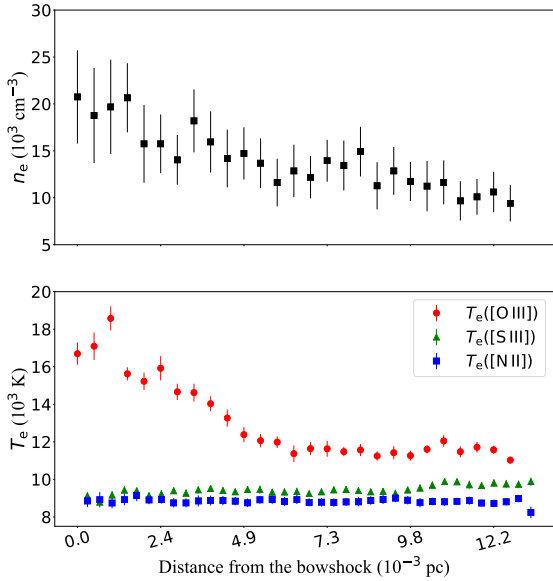


Figure 6: Spatial distribution of physical conditions as a function of the distance to the eastern – external – edge of the bowshock of HH 204. *Upper panel:* n_e ([Fe III]). The gas compresses as it approaches to the shock front, increasing its density. *Bottom panel:* T_e estimates with 3 diagnostics. While T_e ([S III]) and T_e ([N II]) remain unaltered, T_e ([O III]) shows a strong increase when approaching the shock.

portional to the electron density (Hartigan et al. 1987). If we assume that the high- T_e ([O III]) area corresponds to the cooling zone formed after the shock, the fact that T_e ([S III]) and T_e ([N II]) are not affected in the same way, would suggest that the high-ionization degree gas should have a much lower density than the low and medium-ionization degree gas and that both components coexist in HH 204. Although there is evidence of entrainment of material emitting in [O III] CELs feeding HH 204 (see Sec. 8), panels (a) and (b) from Fig. 2 show that the spatial and spectral distribution of [O III] and [O II] do not differ considerably. This fact can indicate two situations, or that there is no gas with two different physical conditions or, on the contrary, both components are intertwined in such a way that our UVES observations cannot separate them.

On the other hand, the kinetic energy of the electrons moving at a velocity $\sim 100 \text{ km s}^{-1}$ relative to the rest frame –as is the case for HH 204– is $\sim 51.8 \text{ eV}$ which is able to ionize an O^+ ion at rest into O^{2+} and excite it to its higher levels. In the bowshock, the difference in velocity between the “target” and the “projectile” gas is

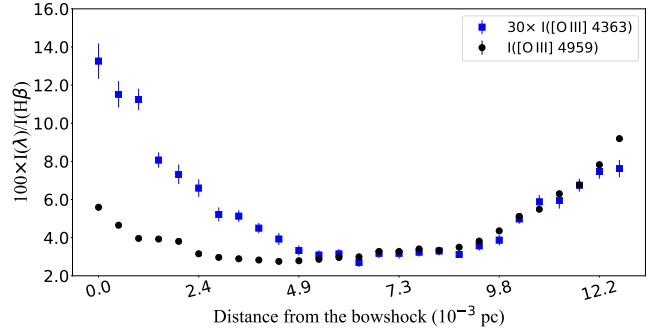


Figure 7: Same as Fig. 6 for the intensities of the [O III] $\lambda\lambda 4363, 4959$ lines. Line intensity ratios with respect to $\text{H}(\beta)$ have been normalized for a clearer comparison.

maximum, and so it would be the shock-ionization and excitation rates to the ${}^1\text{S}_0$ level of O^{2+} . This would create a localized high- T_e ([O III]) zone where temperature would decrease as we move away from the bowshock.

Therefore, we suggest that we are seeing the superposition of two different emission components: one from the bow shock and one from the Mach disk (the shock internal to the jet). The jet shock will have a lower Mach number, \mathcal{M} , than the bow shock so long as the unshocked jet is denser than the ambient medium, as appears to be the case in HH 204. The thickness of the equilibrium (cooled) shocked shell is proportional to \mathcal{M}^{-1} and so should be larger for the shell behind the Mach disk, which thus dominates the emission in much of the slit (displacements 5 to 12 mpc in Fig. 7). At smaller displacements, the contribution of the bow shock (from collisional heating) gets progressively larger, thus explaining the increase in T_e ([O III]). The expected length scale for this variation is roughly the radius of curvature of the bow shock, which agrees with the observed 5 mpc. The only reason that this effect is visible at all is that [O III] emission from the equilibrium shell is so weak. For lower ionization lines, the contribution of the bow shock to the total brightness is always negligible, even for positions close to the shock.

The fact that between 5 to 12 mpc in Fig. 6, T_e ([O III]) reaches an apparent equilibrium at a higher temperature than T_e ([N II]), may be due to the shock contribution of the wings, which are not perpendicular to the direction of propagation of HH 204.

Although part of the aforementioned high-ionization degree gas may be out of photoionization equilibrium, fortunately, its impact is negligible in the global abundance analysis of HH 204. Considering the ionization fraction $\text{O}^{2+}/(\text{O}^+ + \text{O}^{2+}) = 0.005 \pm 0.001$ (see Table 4) – which would increase to $\text{O}^{2+}/(\text{O}^+ + \text{O}^{2+}) = 0.017 \pm 0.003$ if we determine the O^{2+} abundance using T_e ([N II]) – we infer that the contribution of the O^{2+} from the high-

ionization degree gas is around $\sim 1\%$ of the oxygen abundance. A similar result is found for other metals. For example, by considering the solar Ne/O ratio recommended by Lodders (2019) and the Ne^{2+}/O value of HH 204, we estimate that $\text{Ne}^{2+}/\text{Ne} \sim 0.001$. The fact that $T_e(\text{[N II]})$ and $T_e(\text{[S III]})$ are kept in balance in HH 204 along the observed pixels proves that the low and medium-ionization degree gas, which comprises more than $\sim 99\%$ of the total, is in photoionization equilibrium.

5.2. Small-scale patterns in the ionic abundances

Fig. 8 shows the spatial distribution of the ionic abundances of O. As described in Sec. 5.1, the increase of $T_e(\text{[O III]})$ may be related to shock heating. Therefore, we highlight in red the O^{2+} abundances in this area in the bottom panel of Fig. 8. In the upper panel, we show the O^+ abundances along all the distances range and the O ones in the area where $T_e(\text{[O III]})$ remains constant. This panel shows that practically all O is in O^+ form. It should be noted that an increase of a factor of ~ 2 in the O^{2+} abundance would represent less than 1% of the total O, well below the associated uncertainties and, therefore, this increase would be undetected in analyses lacking our spatial and spectral resolutions.

In tables 4 and 5 we can see that the O^+ abundances determined from CELs and RLs for HH 204 are the same within the errors, so we do not find an abundance discrepancy (AD) for this ion, contrary to the situation found in practically all photoionized nebulae. Fig. 9 indicates the absence of any significant AD in all the observed areas of HH 204. Although some fluctuations seem to be present, they are very small in any case. The origin of the AD problem has been related to temperature, density or chemical inhomogeneities in the nebulae or fluorescence effects on the intensity of RLs (and references therein Peimbert 1967; Torres-Peimbert et al. 1980; Liu et al. 2001; Pequignot et al. 1991; García-Rojas & Esteban 2007; Escalante et al. 2012). In relation to this, there are three properties of HH 204 that we want to highlight: (i) In Sec. 5.1, we show that the spatial distribution of $T_e(\text{[N II]})$ is constant, i. e. there are no significant temperature fluctuations in the plane of the sky that may be translated into fluctuations in the line of sight. The presence of temperature fluctuations would produce the underestimation of the O^+ abundance based on CELs. (ii) In Sec. 4.3, we show that the effects of starlight fluorescence are negligible in the determination of the abundances of Ni^+ and Fe^+ due to the large distance between HH 204 and the ionizing source in addition to the high density of the HH object. Thus, if there is any mechanism in which the contin-

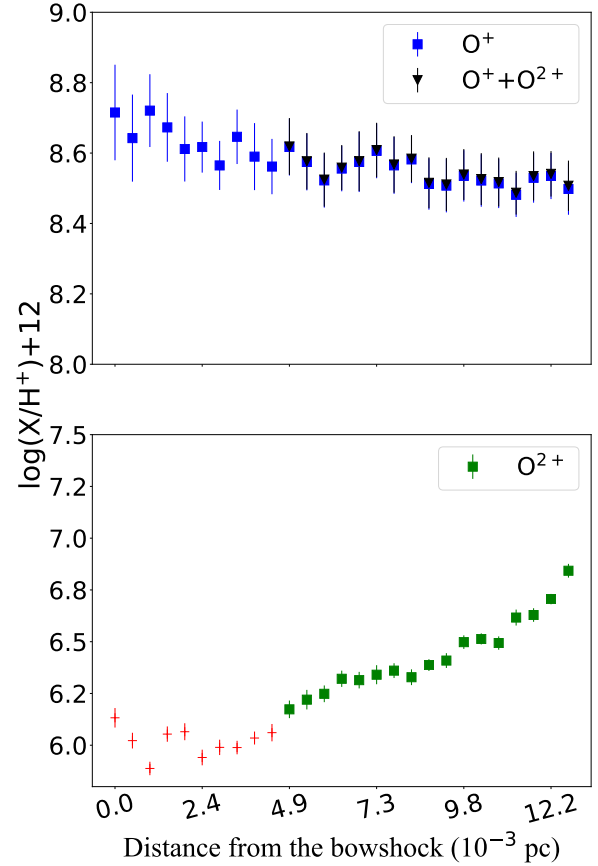


Figure 8: Same as Fig. 6 for ionic and total abundances of O. *Upper panel:* O^+ and total O abundances. The total abundance of O was calculated as the sum of O^+ and O^{2+} in the area where $T_e(\text{[O III]})$ remains constant – distances between 4.9 and 13 mpc from the bowshock –. The contribution of O^{2+} to total O abundance is negligible compared to the abundance of O^+ . *Bottom panel:* O^{2+} abundances. The red crosses show the zone clearly affected by the shock (see Fig. 6, Fig. 7 and Sec. 5.1). The green squares indicate the area where $T_e(\text{[O III]})$ remains constant.

uum pumping can affect the population of the levels of multiplet 1 of O I, this may be diminished in a similar way. Moreover, (Mesa-Delgado et al. 2009) report an $\text{ADF}(\text{O}^+) \sim 0$ in HH 202 S, which is located closer to the ionization source of the nebula, indicating that, in any case, O I lines of multiplet 1 are not likely to be exposed to fluorescence effects due to continuum pumping. (iii) The jet-geometry of HH 204, with a relatively small angle of $32 \pm 6^\circ$ with respect to the plane of the sky (see

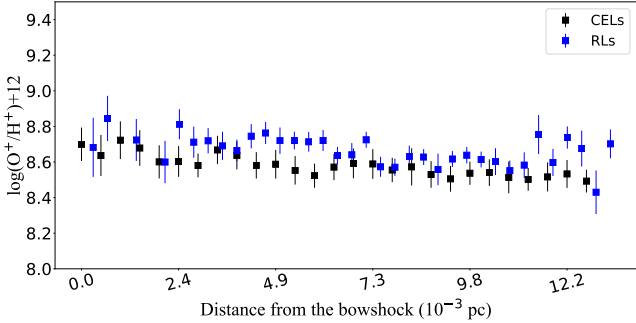


Figure 9: Same as Fig. 6 for O⁺ abundances determined with CELs and RLSs.

Sec. 8), implies that any gradient in the physical conditions along the jet axis should be separated in the plane of the sky. This is a more favorable geometry for analysis than the case of a jet flowing directly towards the observer where different zones will overlap the same line of sight. Therefore, the existence of chemical or density inhomogeneities in the line of sight should not be significant. These three facts favor that the AD(O⁺) is small in HH 204. Unfortunately, we can not perform a similar analysis for the AD(O²⁺) because we do not detect O II RLS in HH 204.

In Fig. 10 we present the ionic abundances of Cl and S. The species of the same ionic charge of both elements show similar pixel by pixel distributions. The variations of S²⁺/H⁺ and Cl²⁺/H⁺ ratios along HH 204 are comparatively much smaller than those of S⁺/H⁺ and Cl⁺/H⁺, that show a decrease of 0.8 dex along the diagram as the distance from the bowshock increases. At distances to the bowshock smaller than ~ 4.9 mpc, the abundances of S⁺ and Cl⁺ seem to stabilize and presumably, almost all S and Cl must be only once and twice ionized. This allows the estimation of their total abundances without an ionization correction factor (ICF).

The pixel by pixel distributions of the ionic abundances of Fe and Ni are clearly correlated, as shown in Fig. 11. Similar to that found for S and Cl (see Fig. 10), close to the bowshock, the contribution of species of Fe and Ni with ionic charges higher than Fe²⁺ and Ni²⁺ to their total abundances should be negligible. The ratios of the ionic abundances between both elements remain constant as shown in Fig. 12, being $\log(\text{Fe}^+/\text{Ni}^+) = 1.26 \pm 0.03$, $\log(\text{Fe}^{2+}/\text{Ni}^{2+}) = 1.37 \pm 0.03$ and $\log(\text{Fe}/\text{Ni}) = 1.33 \pm 0.03$. Although the value of $\log(\text{Fe}^{2+}/\text{Ni}^{2+})$ is slightly above the recommended solar value ($\log(\text{Fe}/\text{Ni})_{\odot} = 1.25 \pm 0.05$ (Lodders 2019)), this may be the consequence of a slight systematic underestimation of Ni²⁺ abundance because, as we

discussed in Sec. 4.3, the atomic data for this ion seems to show some inaccuracies.

In Fig. 13 we show the similar pixel by pixel distributions of the He⁺ and Ar²⁺ abundances. Both quantities decrease as we approach the bowshock due to the decrease of the ionization parameter as n_e and the distance from the ionizing star increases. A slight increase is observed at distances less than ~ 2.4 mpc, probably due to the same process discussed in Sec. 5.1 for the case of [O III] lines. However, the impact of this contribution seems to be negligible for these ions. For example, the fact that $T_e(\text{HeI})$ is consistent with $T_e([\text{N II}])$ (see Sec. 4.1) reflects that the population of the singlet levels, which are the ones used for determining $T_e(\text{HeI})$, are largely unaffected.

In Fig. 14, we show that the abundance of N⁺ increases as we move towards the bowshock from $12 + \log(\text{N}^+/\text{H}^+) = 7.53 \pm 0.03$ to an apparently constant value of 7.75 ± 0.02 . That plateau indicates that all nitrogen should be only once ionized. Figures 15 and 16 show the pixel by pixel distributions of Cr⁺ and Ca⁺ abundances, respectively, which are somewhat different to the ones of Fe⁺ or Ni⁺ (Fig. 11). This makes that the distributions of Fe⁺/Cr⁺ and Fe⁺/Ca⁺ ratios are not constant, contrary to what is obtained for Fe⁺/Ni⁺ (Fig. 17). In the case of the Fe⁺/Cr⁺ ratio, the observed trend may be related to the slight differences between their ionization energies or to different depletion patterns. The curve defined by the Fe⁺/Ca⁺ abundance ratio, may be due to the coexistence of this ion and H⁰ in the ionization front.

5.3. A direct measurement of t^2

Several works have studied the possible existence of small spatial scale variations of temperature in the plane of the sky in the Orion Nebula (O'Dell et al. 2003; Mesa-Delgado et al. 2008; García-Díaz et al. 2008). However, the values of the Peimbert's t^2 (Peimbert 1967) estimated in this way may differ substantially from those defined along the line of sight because of the geometry of the Orion Nebula. Fortunately, this does not seem to be a problem in the case of HH 204. Its jet geometry, propagating at an angle of $32 \pm 6^\circ$ with respect to the plane of the sky (See Sec. 8), implies that the integrated volume in the line of sight should be relatively small. If we assume a geometry of an elliptical paraboloid with the UVES slit located in the projection of the symmetry axis in the sky plane (see Fig. 1), then each pixel will integrate the emission of a representative zone of a disc of gas. Variations in the physical conditions would be expected mostly between adjacent discs, being less likely in the azimuthal direction within

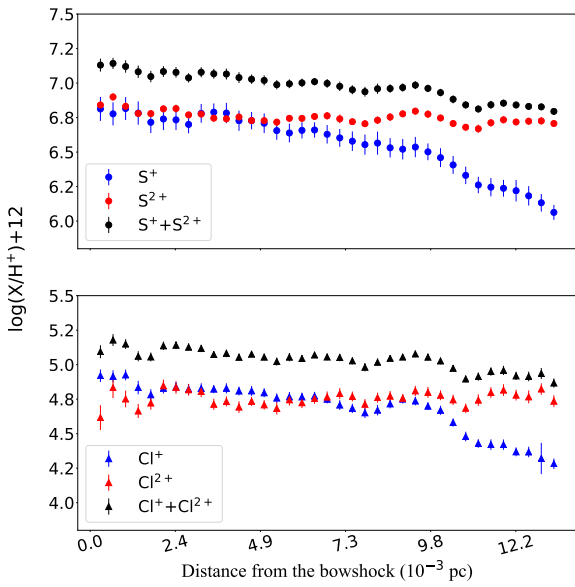


Figure 10: Same as Fig. 6 for ionic abundances of S (upper panel) and Cl (bottom panel).

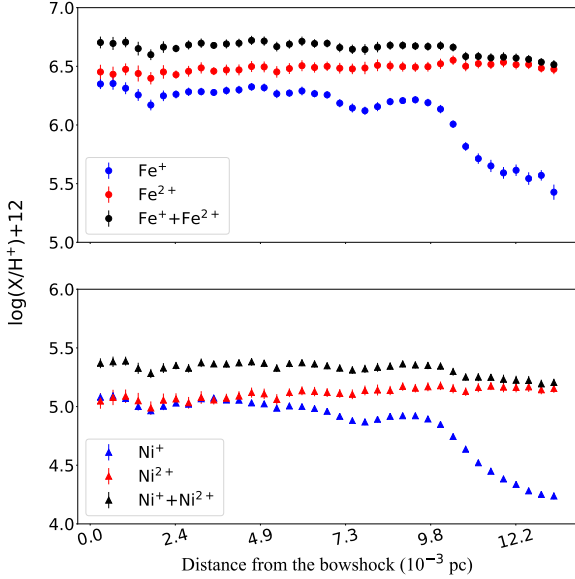


Figure 11: Same as Fig. 6 for ionic abundances of Fe (upper panel) and Ni (bottom panel).

each disc. As discussed in Sec. 5.1, $T_e(\text{[O III]})$ shows strong temperature variations along the observed area of HH 204. Since we know the small-scale distribution of the physical conditions and the O^{2+}/H^+ ratio determined using $T_e(\text{[O III]})$ along the jet, we can apply the

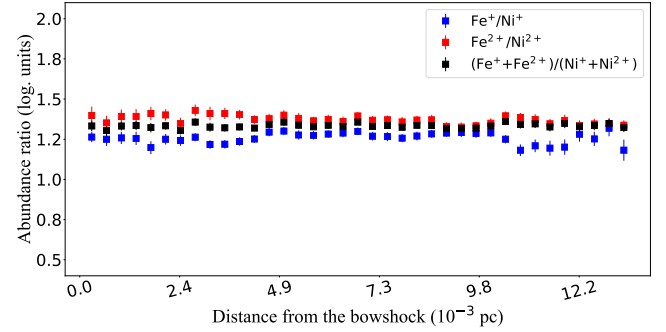


Figure 12: Same as Fig. 6 for the ratios of ionic abundances of Fe and Ni.

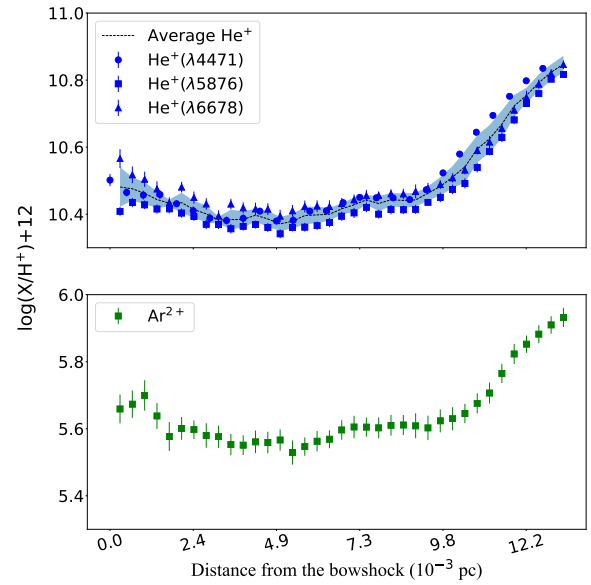


Figure 13: Same as Fig. 6 for He^+ abundances (upper panel) and Ar^{2+} abundances (bottom panel). In the upper panel, the black line indicates the average He^+ abundance obtained with $\text{He I } \lambda\lambda 4471, 5876, 6678$. The color band indicates the associated dispersion.

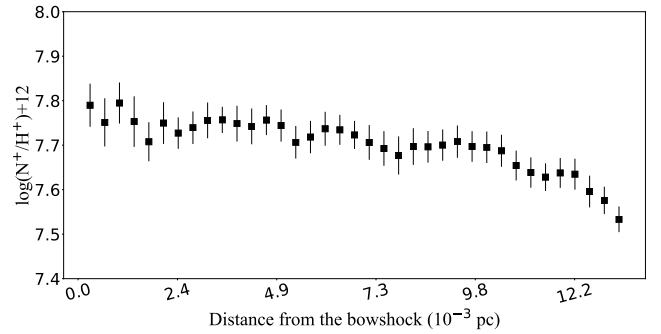


Figure 14: Same as Fig. 6 for N^+ abundances.

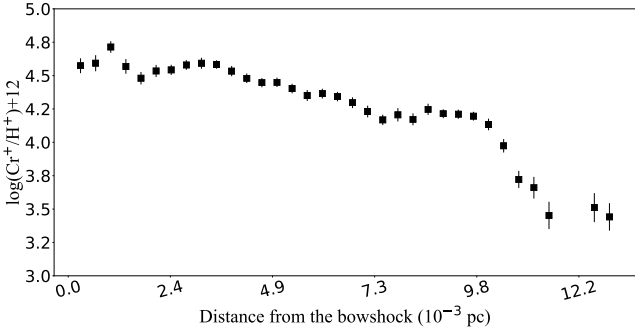


Figure 15: Same as Fig. 6 for Cr⁺ abundances.

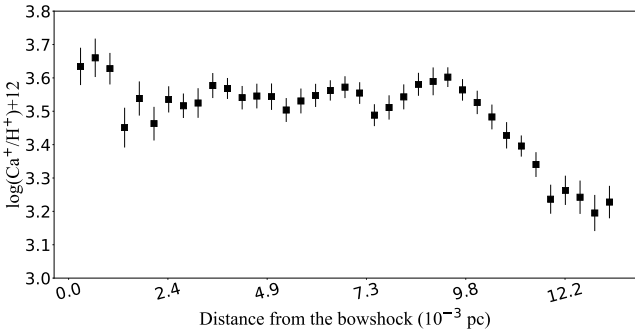


Figure 16: Same as Fig. 6 for Ca⁺ abundances.

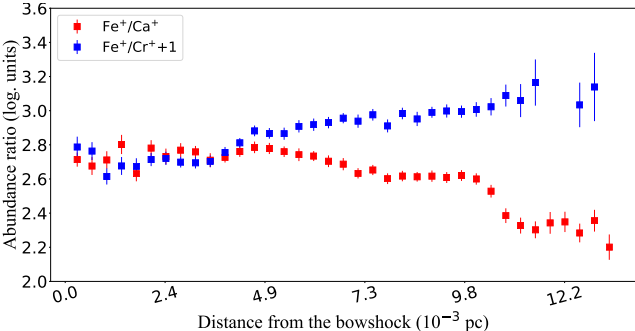


Figure 17: Same as Fig. 6 for Fe⁺/Ca⁺ and Fe⁺/Cr⁺ abundance ratios.

formalism developed by Peimbert (1967) for estimating $t^2(O^{2+})$ and $T_0(O^{2+})$ directly from the definition. Eqs. 9 and 12 from Peimbert (1967), are solved below, by assuming the aforementioned geometry:

$$T_0 = \frac{\int T_e n_e n(O^{2+}) dV}{\int n_e n(O^{2+}) dV} \approx \frac{\sum_{l=0}^{l=d} T_e n_e n(O^{2+}) l^{1/2} \Delta l}{\sum_{l=0}^{l=d} n_e n(O^{2+}) l^{1/2} \Delta l}, \quad (2)$$

$$\begin{aligned} t^2 &= \frac{\int (T_e - T_0)^2 n_e n(O^{2+}) dV}{T_0^2 \int n_e n(O^{2+}) dV} \\ &\approx \frac{\sum_{l=0}^{l=d} (T_e - T_0)^2 n_e n(O^{2+}) l^{1/2} \Delta l}{T_0^2 \sum_{l=0}^{l=d} n_e n(O^{2+}) l^{1/2} \Delta l}, \end{aligned} \quad (3)$$

where l is the distance variable along the jet axis and d is ~ 13 mpc, the maximum observed distance from the bowshock to the edge of the slit. The amplitude of the curvature of the bowshock and the angle of the jet with the plane of the sky are canceled out. The results are $T_0(O^{2+}) = 12040 \pm 80$ K and $t^2(O^{2+}) = 0.012 \pm 0.002$. This is probably the first tentative measurement of t^2 that may be representative for the integrated gas volume of an ionized nebular object. Comparing the results with Eq. 15 from Peimbert (1967), we obtain that the expected $T_e([O\text{ III}])$ we would obtain adding all the pixels considered in the pixel by pixel analysis is 12390 ± 80 K, in agreement with the results of Sec. 4.1 (see Table 3), fact that validates our assumptions. Therefore, in our case, temperature variations of the order of 10^3 K do not break the validity of approximating the temperature-dependence of the emissivity of CELs through the first terms of a Taylor series, and can be properly characterized with Peimbert's t^2 formalism.

5.4. Deuterium lines in HH 204

The emission of deuterium lines in the Orion Nebula was initially recognized by Hébrard et al. (2000a). Unlike the expected isotopic shift of -81.6 km s $^{-1}$ with respect to the hydrogen lines, they observed a shifted emission around ~ -71 km s $^{-1}$ from H α and H β . The difference of ~ 10 km s $^{-1}$ is essentially due to the fact that their emission is produced in different areas of the nebula, where the bulk of gas is moving at different radial velocities. Since the hydrogen lines are produced by recombination in the ionized area that expands towards the observer, the deuterium emission is mainly due to fluorescence excitation with non-ionizing far-UV continuum in areas slightly beyond the ionization front, as the photon dominated region (PDR) or in the H I-H II interface (O'Dell et al. 2001). After the recognition of the deuterium emission in the Orion nebula, this was also identified in other H II regions such as M8, M16, DEM S 103, M20 and S 311 (Hébrard et al. 2000b; García-Rojas et al. 2005, 2006, 2007). As in the Orion Nebula, the deuterium emission in these H II regions has a narrow line width, consistent with their origin in colder areas.

In this work, we detect the emission of D ζ , D ε , D δ , D γ , D β and D α as shown in Fig. 18. In Table 6 we present the characteristics of these emissions. The observed isotopic shift of -81.4 km s $^{-1}$ between deuterium and hydrogen lines indicates that both kinds of lines arise from HH 204. The observed DI/HI intensity ratios are in good agreement with the predictions of the standard model developed by O'Dell et al. (2001) for the Orion Nebula, confirming the fluorescent nature of

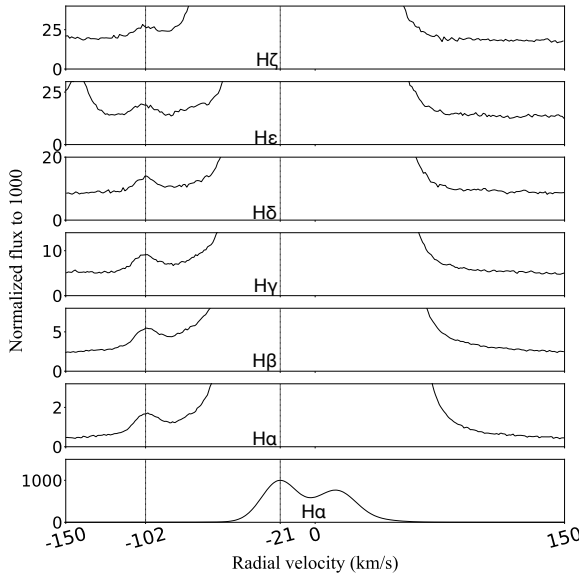


Figure 18: Deuterium lines observed in the spectra of cut 1. Vertical lines indicate the position of the deuterium lines and the HI emission from HH 204. The flux is normalized to the peak emission of HH 204 in each case.

the DI emission. Considering that the emission of deuterium occurs in areas slightly beyond the ionization front, the detection of these lines implies that the ionization front must be trapped in HH 204, moving along with it, in consistency with the results of Núñez-Díaz et al. (2012), as well as other evidence that will be discussed in Sec. 9.3.

5.5. Sub-arcsecond imaging of HH 204

Fig. 19a shows the ratio of surface brightnesses, $R([\text{O III}]) = S([\text{O III}] \lambda 5007)/S(\text{H}\alpha \lambda 6563)$, calculated from *HST* WFPC2 observations in the F502N, F547M, F656N, and F658N filters from program GO5469 (O'Dell & Wong 1996). It can be seen that the line ratio in the background nebula shows a pronounced gradient from $R([\text{O III}]) \approx 0.3$ in the north-east to $R([\text{O III}]) \approx 0.5$ in the south-west.³ Inside the bow shock, the ratio is significantly smaller, for instance falling from $\simeq 0.4$ to $\simeq 0.2$ along the length of the UVES slit.

However, the most interesting feature of the $R([\text{O III}])$ image is the slight *increase* in the ratio that is seen in a

thin layer along the leading edge of the bow shock. This is most clearly visible in the northern wing of HH 204, such as the area highlighted by a dotted outline box in the figure. Average profiles across the shock for this region are shown in Fig. 19b. The lower panel shows that the raw ratio (solid black line) increases only slightly above its value in the background nebula, which is because the brightness increase across the bow shock is only a small fraction of the background brightness, as can be appreciated in the upper panel. In order to isolate the emission of the shocked gas from that of the nebula, we calculate the background-subtracted line ratio:

$$R'([\text{O III}]) = \frac{S([\text{O III}]) - S_{\text{BG}}([\text{O III}])}{S(\text{H}\alpha) - S_{\text{BG}}(\text{H}\alpha)} \quad (4)$$

under the assumption that S_{BG} for each line is constant along the profile. The result is shown as a gray histogram in the lower panel of the figure, which reveals a sharp peak of width ≈ 0.3 mpc that reaches a maximum value $R'([\text{O III}]) \approx 2R_{\text{BG}}([\text{O III}])$ and is centered on a displacement of ≈ -0.1 mpc. The origin of the displacement axis is set to the peak in the spatial gradient of the $\text{H}\alpha$ surface brightness, corresponding to the outer edge of the dense shocked shell. The negative displacement of the $R'([\text{O III}])$ peak means that this occurs *outside* the dense shell, closer to the shock front itself.

Fig. 19c shows the same quantities calculated along a cut that coincides with our UVES slit at the head of HH 204. In this case, $R'([\text{O III}])$ is always significantly less than $R_{\text{BG}}([\text{O III}])$, but it does still show a small local peak with a position and width that is similar to the more impressive one in the northern wing. These peaks in $R'([\text{O III}])$ occur over a much smaller scale than any of spatial gradients that we find in our UVES slit spectra and are only detectable because of the high spatial resolution of the *HST*.⁴ For example, the increase in $T_e([\text{O III}])$ that we detect in the blue-shifted emission near the shock front (Fig. 6) occurs over a scale of 5 mpc, indicated by the red arrow in the figure, which is more than 10 times larger than the width of the $R'([\text{O III}])$ peak.

What is the origin of the narrow peak in the $[\text{O III}]/\text{H}\alpha$ ratio that is seen just outside the shocked shell? When a shock propagates into low-ionization gas (predominantly O^+), there are three zones where enhanced $[\text{O III}]$ emission might be expected (Cox & Raymond 1985; Sutherland & Dopita 2017): first, the radiative precursor in the pre-shock gas; second, the non-equilibrium collisional ionization zone immediately after the shock; third, the

³ For comparison with results from our UVES spectra, and using the average reddening for the HH 204 region (Weillbacher et al. 2015), the conversion is $\lambda 4959/\text{H}\beta \approx 1.1R([\text{O III}])$.

⁴ Pixel size of 0.045 arcsec, which well samples the PSF width at $\text{H}\alpha$ of 0.083 arcsec.

Table 6: Characteristics of deuterium and hydrogen lines in HH 204.

λ_0	v_r (km s $^{-1}$)	DI		HI		$I(DI)/I(HI) \times 1000$
		FWHM (km s $^{-1}$)	v_r (km s $^{-1}$)	FWHM (km s $^{-1}$)	$I(DI)/I(HI) \times 1000$	
3889.05*	-103.34	13.80 ± 1.39	-	-	-	-
3970.07	-103.10	14.20 ± 3.40	-21.54	24.62 ± 0.02	2.99 ± 0.45	
4101.73	-102.83	13.53 ± 0.86	-20.97	24.49 ± 0.01	2.24 ± 0.15	
4340.46	-103.02	16.17 ± 1.40	-20.83	24.66 ± 0.01	2.10 ± 0.16	
4861.32	-102.26	14.31 ± 1.90	-21.47	24.67 ± 0.01	1.06 ± 0.11	
6562.80	-101.82	14.90 ± 0.79	-21.88	24.94 ± 0.01	0.58 ± 0.03	

NOTE—* The HI $\lambda 3889.05$ emission of HH 204 is blended with the nebular one of He I 3888.65

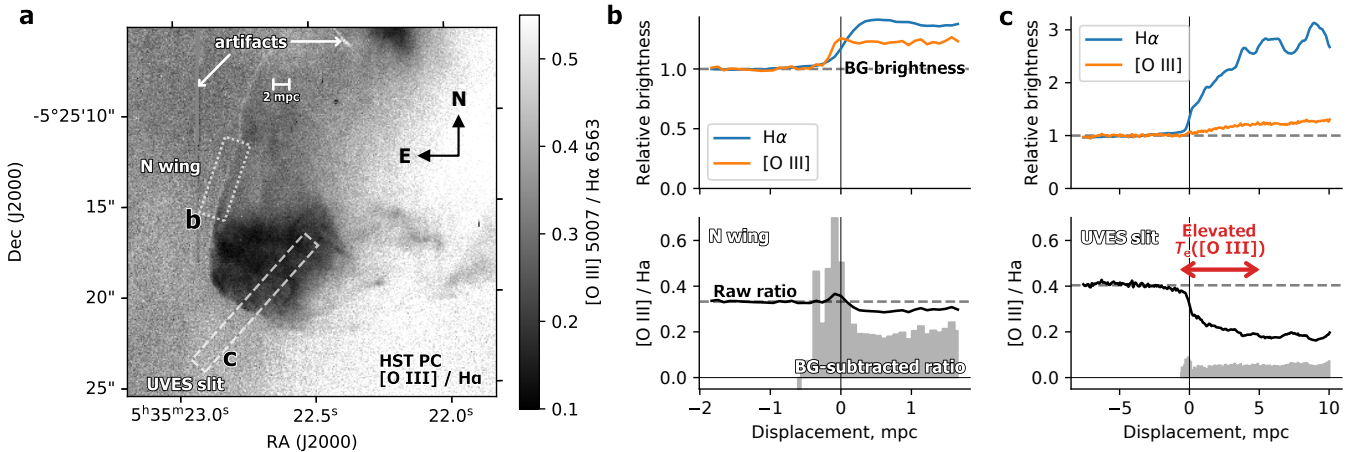


Figure 19: (a) Map of the line ratio $[O\text{ III}]\lambda 5007/\lambda 6563$, calculated from *HST* images with the PC chip of the WFPC2 camera. The position of the UVES spectrograph slit is outlined by a dashed box, while a further region of interest in the N wing of the bow shock is indicated by a dotted box. The vertically oriented “scar” at upper left is an artifact due to the bright star θ^2 Ori A, located just north of the field of view. (b) Average cut profiles of the *HST* images for the box in the N wing that is outlined in panel a. Upper graph shows surface brightness profiles in the two emission lines, normalized to the mean nebular background value outside of the shock. Lower graph shows the line ratio, with the raw ratio indicated by the black solid line and the background-subtracted ratio indicated by the gray histogram. The zero point of the displacement axis is taken to be the location of the maximum gradient in the $H\alpha$ surface brightness. (c) Same as panel b, but showing average profiles of the *HST* images along the UVES slit. The region of the slit that shows $T_e([O\text{ III}]) > 12\,000\text{ K}$ in the blueshifted component is indicated by the red arrow.

radiative relaxation zone where the post-shock gas cools back down to the photoionization equilibrium temperature of $\sim 10^4\text{ K}$. The first of these can be ruled out in the case of HH 204 because the pre-shock photoionization of O^+ would require shock velocities greater than 150 km s^{-1} , observed proper motion and radial velocities imply a shock velocity around 100 km s^{-1} . The second zone has a high temperature ($> 50\,000\text{ K}$ for shock velocities $> 55\text{ km s}^{-1}$) but is severely under-ionized, resulting in line emissivities that are far in excess of the equilibrium values in a very thin layer. The third zone, in which oxygen is recombining through the O^{++} stage

while cooling through the range $30\,000\text{ K}$ to $10\,000\text{ K}$ is predicted to be somewhat thicker and with a higher electron density, yielding a greater contribution to the total $[O\text{ III}]$ emission. Given the electron density that we derive of $13\,500\text{ cm}^{-3}$ (Table 3), and assuming a shock velocity $< 70\text{ km s}^{-1}$, the cooling length should be approximately 0.05 mpc , or 0.025 arcsec , which is a few times smaller than the *HST* resolution. However, this analysis applies only to the head of the bow shock. In the wings, the shock is not perpendicular to the upstream gas velocity, but is oblique at an angle α . This yields a post-shock equilibrium density that is smaller by a fac-

tor of $\cos^2 \alpha$, and a cooling length that is larger by the same factor. Hence, the cooling length is expected to be resolved for α smaller than about 45° , which is consistent with our observations of the narrow peak in the [O III]/H α ratio in the north wing. The reason that the same behaviour is not seen in the opposite wing is probably that the ambient nebular emission is much more highly ionized there, which masks the effect.

6. TOTAL ABUNDANCES

In the case of the nebular and the DBL components, total abundances of O, Cl, and S were estimated by simply adding the abundances of all their observed ions. Although there may be some contribution of S $^{3+}$ and Cl $^{3+}$, the ICFs of Stasińska (1978) and Esteban et al. (2015), respectively, predict negligible amounts of those species. In the case of N, Ne, Ar and C, we adopt the same ICFs used by Arellano-Córdova et al. (2020). For Fe, we use the two ICFs proposed by Rodríguez & Rubin (2005). Since the real value of Fe should be between the predictions of both ICFs (Rodríguez & Rubin 2005), in Table 7 we present those determinations as lower and upper limits of the Fe abundance.

In the case of HH 204, based on the results of Sec. 5, we decided not to derive total abundances of elements for which we only observe highly ionized ions, such as He, Ne, Ar and C, due to the low ionization degree of the gas and the large contribution of the ICFs. In the cases of O, N, Cl, S, Fe and Ni, we can determine their total abundances without ICFs. As seen in Sec. 5, the spatial distribution of the abundances of the once and twice ionized ions of Cl, S, Fe and Ni reach constant values at positions close to the bowshock, where the degree of ionization becomes very low. In this zone, the contribution of three – or more – times ionized ions of these elements should be negligible. A similar situation occurs with N, where the contribution of N $^{2+}$ is expected to be very small close to the bowshock. Therefore, in Table 7 we present the total abundances obtained by adding the mean abundances of the once and twice ionized ions of Cl, S, Fe and Ni for distances less than 4.9 mpc from the bowshock. In the case of O and N, we only consider the abundance of once ionized ions in the same range of distances. At these distances, the pixel by pixel values of the O $^+$ abundance determined from RLs have large errors (see Fig. 9), because of the faintness of OI $\lambda 7772$ line. In this case, we use the O $^+$ abundance obtained from the integrated spectrum presented in Table 4 to determine the total O abundance based on RLs.

7. THE EFFECTS OF LOWERING THE SPATIAL AND SPECTRAL RESOLUTION

In Sec. 5, we have carried out a pixel by pixel analysis of the physical conditions and ionic abundances of the ionized gas in HH 204, separating the different kinematical components. In this section, we perform a completely different kind of analysis, simulating a spectrum with lower spatial and spectral resolution. Contrary to the case studied in Paper I, where the components of HH 529 II and HH 529 III are fainter than the emission of the Orion Nebula, HH 204 is a quite brighter object, with an intensity similar to that of the nebular component. Therefore, the contribution of HH 204 to the integrated low-spectral resolution spectrum is significant. We define a new spectrum by adding the flux of all the velocity components, which includes the emission of HH 204, the DBL and the emission of the Orion Nebula along the whole UVES slit. Following the reddening correction procedure described in Sec. 3, we obtain $c(\text{H}\beta) = 0.36 \pm 0.02$ for this integrated spectrum.

In Fig. 20, we present the resulting plasma diagnostics of the low-resolution spectrum. This diagram can be compared with those of the individual components, shown in Fig. 24. If one only has the information provided by this degraded spectrum, and applies the classic procedure of averaging $n_e(\text{[O II]})$, $n_e(\text{[S II]})$ and $n_e(\text{[Cl III]})$ – excluding $n_e(\text{[Fe III]})$, since the sometimes discrepant values given by this diagnostic are generally interpreted as the effect of incorrect atomic data – we would obtain $n_e = 3430 \pm 580$. Using this value of density, we would obtain $T_e(\text{[O II]}) = 12140_{-930}^{+950}$ K, $T_e(\text{[S II]}) = 19220_{-2530}^{+9020}$ K, $T_e(\text{[N II]}) = 9200 \pm 200$ K, $T_e(\text{[S III]}) = 8740_{-200}^{+230}$ K and $T_e(\text{[O III]}) = 8530_{-120}^{+100}$ K. It must be noted that the resulting $T_e(\text{[N II]})$ is higher than the ones obtained for each individual component analyzed in Sec. 4.1. Moreover, $T_e(\text{[O II]})$ and $T_e(\text{[S II]})$, the most density-dependent diagnostics, show much higher values. However, their effect on abundance determinations could be somehow mitigated, as their associated uncertainties are very high and the use of a weighted mean of the different temperature indicators would reduce their contribution. $T_e(\text{[N II]})$ has always much lower uncertainties and is generally the preferred temperature diagnosis for low-ionization degree ions.

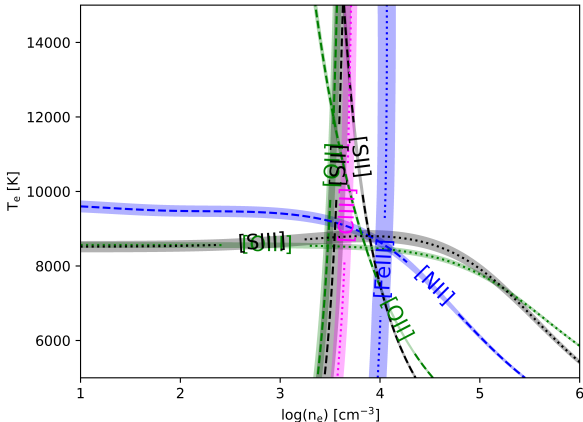
Following the usual procedure and assuming the physical conditions determined in the previous paragraph, we would determine the O $^+$ abundance using $T_e(\text{[N II]})$ and the O $^{2+}$ one with $T_e(\text{[O III]})$, obtaining O $^+ = 8.15 \pm 0.04$, O $^{2+} = 7.63 \pm 0.02$ and a total abundance of O = 8.26 ± 0.03 . This value of the O/H ratio is lower than the one determined for all the individual components. The only exception could be the DBL in cut 2, which shows O = 8.31 ± 0.12 (see Table 7), whose uncertainty is large enough to encompass the value obtained for the

Table 7: Total abundances.

Element	Cut 1		Cut 2	
	HH 204	Nebula + DBL	DBL	Nebula
O	8.62 ± 0.05	8.36 ± 0.03	8.31 ± 0.12	8.42 ± 0.04
O*	8.57 ± 0.03	-	-	-
N	7.75 ± 0.02	7.56 ^{+0.04} _{-0.03}	7.45 ^{+0.09} _{-0.08}	7.53 ± 0.05
Ne	-	7.56 ± 0.04	-	7.61 ± 0.05
S	7.07 ± 0.03	6.90 ± 0.03	6.90 ± 0.09	6.94 ± 0.04
Cl	5.10 ± 0.04	5.00 ± 0.03	5.04 ± 0.14	5.03 ± 0.05
Ar	-	6.14 ± 0.02	6.09 ± 0.10	6.17 ± 0.02
Fe	6.67 ± 0.03	5.91-6.09	5.64-6.19	5.97-6.13
Ni	5.35 ± 0.03	-	-	-
C*	-	8.49 ± 0.05	-	8.64 ± 0.04

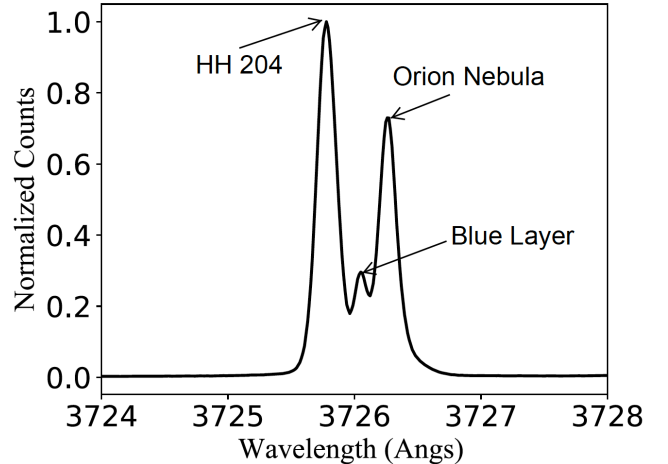
NOTE—Abundances in units of 12+log(X/H).

* Based on RLs.

**Figure 20:** Plasma diagnostics of the spectrum defined by adding all the observed velocity components along the whole UVES slit.

low resolution spectrum. However, this does not mean the DBL dominates the observed abundance of O, since it is the weakest component. This is demonstrated in Fig. 21, which shows the line profile of $f([O\text{ II}]\lambda 3727)$, one of the most intense lines in the spectrum of the DBL.

The explanation of the low O abundance in the low resolution spectrum is due to the use of the classical procedure to estimate n_e . The classical density diagnostics do not adequately account for the high density of HH 204. The critical densities of the levels involved in those diagnostics are below the density of HH 204 (see Table D5 of Paper I). Likewise, the sensitivity of $I([O\text{ II}]\lambda 3726)/I([O\text{ II}]\lambda 3729)$ and $I([S\text{ II}]\lambda 6731)/I([S\text{ II}]\lambda 6716)$ at $n_e \sim 10^4 \text{ cm}^{-3}$ is

**Figure 21:** Normalized $f([O\text{ II}]\lambda 3727)$ in the spectrum that results from adding all the spatial pixels in the UVES slit. Each of the velocity components are identified.

much lower than at $n_e \sim 10^2 - 10^3 \text{ cm}^{-3}$, the normal range of densities in H II regions. The degree of ionization of each component also plays an important role. Although $I([Cl\text{ III}]\lambda 5538)/I([Cl\text{ III}]\lambda 5518)$ is more density sensitive than $I([O\text{ II}]\lambda 3726)/I([O\text{ II}]\lambda 3729)$ or $I([S\text{ II}]\lambda 6731)/I([S\text{ II}]\lambda 6716)$ at densities of around $n_e \sim 10^4 \text{ cm}^{-3}$, HH 204, –the component with the highest density– has a very low degree of ionization. Therefore, in the combined emission of HH 204 and the Orion Nebula, the second component has a greater weight in $n_e([Cl\text{ III}])$. On the other hand, $I([Fe\text{ III}]\lambda 4658)/I([Fe\text{ III}]\lambda 4702)$ is practically insensitive at densities smaller than $n_e \sim 10^3 \text{ cm}^{-3}$, and the

critical density of this diagnostic is above $\sim 10^6 \text{ cm}^{-3}$. In addition, most of the [Fe III] emission comes from HH 204 due to its higher abundance of gaseous Fe with respect to the Orion Nebula and the DBL. These properties makes it an excellent indicator of the presence of high-density gas as HH objects. In our case, the $n_e(\text{[Fe III]}) = 10790_{-2620}^{+3230} \text{ cm}^{-3}$ we obtain for the low resolution spectrum is rather close to the density of HH 204. This confirms the importance of the warning given by Morisset (2017) who, through photoionization models, predict large errors in the determination of the physical conditions and chemical abundances in nebulae if one assumes a single component when, in fact, there are several and some of them is composed by high-density gas. The exercise we present in this section is an observational confirmation.

Another interesting aspect is the behavior of the O RLs in the low-resolution spectrum. Unfortunately, the O I RLs from multiplet 1 can not be studied in this spectrum since the nebular emission is deeply affected by sky features. On the other hand the O II RLs do not have this problem. After our previous analysis, we know that the contribution of HH 204 and the DBL to the total O II emission is negligible. However, in a low resolution spectrum we would not know this *a priori*. This can be revealed by the resulting $n_e(\text{O II})$, obtained from the line ratios of O II multiplet 1, which essentially will give the conditions of the Orion Nebula $n_e(\text{O II}) \sim 1500 \text{ cm}^{-3}$, a factor 2 lower than those already underestimated $n_e(\text{[O II]})$ and $n_e(\text{[S II]})$. In this low-resolution spectrum, since the O²⁺ emission essentially comes from the Orion Nebula, and $T_e(\text{[O III]})$ is rather insensitive to the chosen density at values smaller than $\sim 10^5 \text{ cm}^{-3}$, the ADF(O²⁺) is practically the same as the one derived in the Orion Nebula. However, this is not the expected case for ADF(O⁺), where the temperature for the ions with low ionization degree is density-dependent.

If instead of using the classical diagnostics to determine n_e , we consider the average of the densities obtained for each component (See Table 3), weighted by their observed $f(\text{H}\beta)$, we get: $n_e = 6820 \pm 810 \text{ cm}^{-3}$. This value is roughly between the predictions of classical diagnostics and $n_e(\text{[Fe III]})$. Note that in Fig. 20, close to this value of density, $T_e(\text{[O II]})$ and $T_e(\text{[S II]})$ converge to $T_e(\text{[N II]})$. Using that density, we obtain: $T_e(\text{[O II]}) = 8650_{-520}^{+410} \text{ K}$, $T_e(\text{[S II]}) = 9890_{-990}^{+1100} \text{ K}$, $T_e(\text{[N II]}) = 8850_{-180}^{+210} \text{ K}$, $T_e(\text{[S III]}) = 8800_{-160}^{+250} \text{ K}$ and $T_e(\text{[O III]}) = 8490_{-120}^{+90} \text{ K}$. Calculating the ionic abundances of oxygen with these physical conditions, we obtain: $\text{O}^+ = 8.36_{-0.05}^{+0.06}$ and $\text{O}^{2+} = 7.64 \pm 0.02$, which

implies $\text{O} = 8.44 \pm 0.05$. Values more consistent with those of the individual components.

The effects of what has been discussed in this section can be clearly observed in Fig. 2 from O'Dell et al. (2017a). That figure shows the spatial distribution of $n_e(\text{[S II]})$ and $T_e(\text{[N II]})$ derived in a pseudo-slit created with MUSE 2D spectroscopic data (Weilbacher et al. 2015), covering a zone close to our observations, but with lower spectral resolution and integrating the emission of HH 204, the DBL and the nebular gas. It can be seen that as one approaches the bowshock from the direction of the jet, $n_e(\text{[S II]})$ increases, reaching a zone where its value stabilizes around $\sim 5000 \text{ cm}^{-3}$ and decreasing again as one moves outwards the bowshock. On the other hand, $T_e(\text{[N II]})$ initially fluctuates at around $\sim 8500 \text{ K}$ but once we are in the area where $n_e(\text{[S II]})$ is high and constant, $T_e(\text{[N II]})$ begins to increase, until reaching a maximum value of $\sim 9500 \text{ K}$. Once the density drops, $T_e(\text{[N II]})$ again reaches values that fluctuate around $\sim 8500 \text{ K}$. A similar behavior was observed by Mesa-Delgado et al. (2008) and Núñez-Díaz et al. (2012) at the edge of the bowshock of HH 204. Those authors associate the peak in $T_e(\text{[N II]})$ with shock heating of the gas.

What actually happens in Fig. 2 of O'Dell et al. (2017a) is that $n_e(\text{[S II]})$ – the density diagnostic they use – is not able to effectively account for the increase in density due to the compression of the gas in HH 204. As shown in Fig. 6, when approaching the bowshock, the density of HH 204 steadily increases up to $\sim 20000 \text{ cm}^{-3}$ at the bowshock, not a zone of stabilization of density when one approaches the bowshock (located around the value 3.2 on the x-axis of Fig. 2 from O'Dell et al. 2017a). As $T_e(\text{[N II]})$ diagnostic tends to be density sensitive for values larger than $\sim 1000 \text{ cm}^{-3}$, an underestimate of n_e implies an overestimate of T_e and consequently, we will obtain significantly lower ionic abundances based on CELs, which intensity is strongly dependent on temperature.

In the case of our observations, the different density components have different radial velocities, which – fortunately – can be separated thanks to our high spectral resolution. However, one might wonder how many internal jets or gas clumps having velocities similar to that of the bulk of the ionized gas can exist in the Orion Nebula. These unresolved components – that would in fact be most likely undetectable – would be integrated along the line of sight and might affect the determination of the true physical and chemical properties of the nebula. It is clear that the discrepancy between the different density diagnostics is not necessarily an artifact of the atomic data used. Instead, each diagnostic may be

revealing differently the changing conditions of the gas integrated along the line of sight of the spectrum. Relying uncritically only on those density diagnostics that are consistent with each other could lead to significant systematic errors.

8. ORIGIN OF THE JET THAT DRIVES HH 204

At least two different high-velocity flows converge on the general HH 203/204 region from the direction of the inner Orion Nebula (see Fig. 22), but it is not clear if either of them are directly responsible for driving the HH 204 bow shock. One flow is at a position angle (PA) of $\approx 118^\circ$ and transitions from a high ionization state north-west of the Bright Bar (cyan contours in Fig. 22a), to a lower ionization state (yellow contours) to the south-east of the Bright Bar. The other is at PA $\approx 140^\circ$ and is of low ionization for its entire detected length. Both these flows give the appearance of driving HH 203, which implies that HH 203 may be a superposition of two unrelated bow shocks. Such a superposition is consistent with the detection of two different velocity components (-73 and -39 km s^{-1}) at the head of the bow shock, and also with the complex structure apparent in high-resolution *HST* images (see Fig. 22b). O'Dell et al. (2015) noted that in addition to the main bow shock (HH 203a), there appears to be a second faint bow shock (HH 203b), associated with the PA118 flow. We also detect a third faint bow shock, which we denote HH 203c, situated in front (SW) of HH 204a. Note that O'Dell et al. (2015) give position angles of 124° and 127° , respectively, for HH 203 and HH 204, which probably represent an average of the PA118 and PA140 flows.

The southern portion of HH 203a, which we label as “[S II] knot” in the figure, is particularly strong in the [S II] and [O I] filters and coincides with the peak of the -39 km s^{-1} feature. The spatial alignment and the similarity in velocity and ionization makes it likely that this knot is part of the PA140 flow. It is conceivable that this flow may extend farther to the SW and be driving the HH 204 bow shock, although there is no direct evidence for this. On the other hand, a third flow at PA $\approx 108^\circ$ is seen to feed into HH 204 from the west. This jet, first noted by Doi et al. (2004), is very short and stubby, and can be traced back only 10 arcsec (20 mpc) from the bow shock. There is another faint filament of high-velocity [O III] emission that extends between the HH 203 and HH 204 regions at PA $\approx 108^\circ$ (see Fig. 22a). This appears to provide a connecting bridge between the PA140 and PA108 flows, although the difference in velocity and ionization with respect to the PA108 flow argues against a physical association with HH 204.

We have searched archival observations in other wavebands for any evidence of jets along the back projection of the PA108 axis. The most convincing association is with a molecular hydrogen filament seen in the $2.12 \mu\text{m}$ line (see Fig. 22e). At the position of this filament, HH 204 is at PA = 105° , which is well within the uncertainties, and the orientation of the filament is consistent with the same PA. Unfortunately, no kinematic observations are currently available for this filament, so its association with HH 204 can only be tentative. The stellar source that best aligns with the H₂ filament is COUP 484, see Fig. 22e. However, this is a rather low luminosity star and therefore seems an unlikely candidate for driving such an impressive large-scale outflow. The star V2235 Ori is also marginally consistent within the uncertainty with the PA108 axis and is roughly 100 times brighter than COUP 484 in the K and L infrared bands (Muench et al. 2002), but its position is completely inconsistent with being the source of the H₂ filament. There is also marginal evidence from MUSE observations (Weilbacher et al. 2015) for a blue-shifted [Fe III] filament that extends from the position of the H₂ filament towards HH 204, but the data are noisy.

A further important line of evidence for the flow direction is provided by proper motion measurements. We have re-measured the proper motions using *HST* images over an interval of 19 years (1996 to 2015) using the methodology described in section 1 of Paper I. For the “nose” of the HH 204 bow shock, we find a plane-of-sky velocity of $(71 \pm 9) \text{ km s}^{-1}$ at PA = $(136 \pm 3)^\circ$. After correcting to a common distance of 417 pc the previous measurements of Doi et al. (2002) are $(83 \pm 10) \text{ km s}^{-1}$ at PA = $(137 \pm 7)^\circ$, which are consistent with our measurements within the uncertainties. The proper motion axis is shown by a large red arrow in Figure 22b for comparison with the candidate axes from the high radial velocity jets. It is marginally consistent with the PA140 axis, but not all with the PA108, PA118, or PA164 axes.

In summary, convincing evidence for which large scale flow might be driving the HH 204 bow shock is frustratingly absent. Although the PA108 flow is clearly associated with HH 204, its short length means that the exact orientation is very uncertain. The PA140 flow has a much better defined direction, but its extension beyond the position of the [S II] knot in order to feed into the HH 204 bow shock is purely speculative. However, the close agreement between this flow direction and the proper motion axis is an additional argument in its favor. The only thing that can be said with any degree of certainty is that the high-ionization PA118 flow is *not* driving HH 204, but only HH 203.

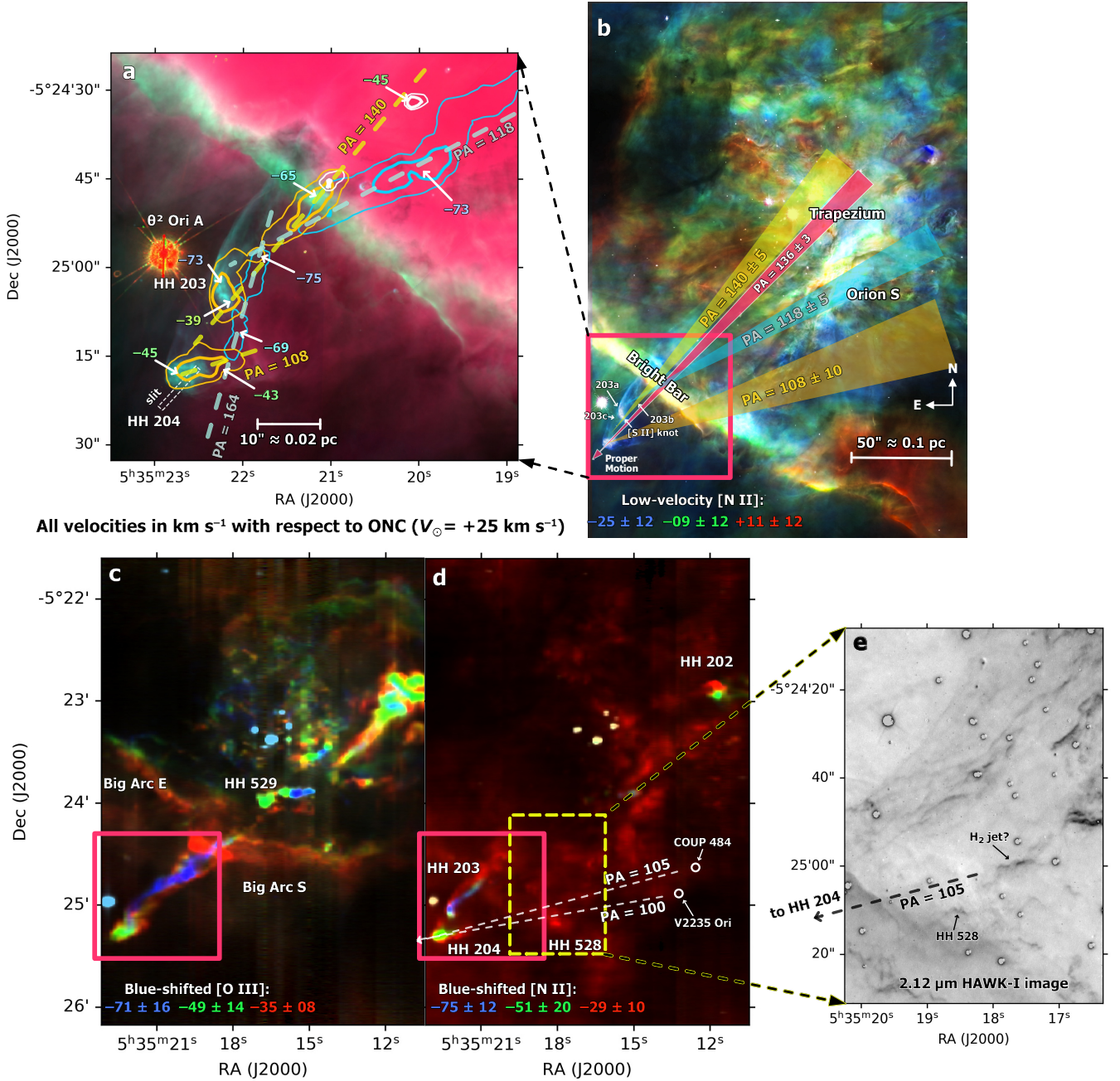


Figure 22: Location of HH 204 within the Orion Nebula. (a) Same as Fig. 1 but showing an expanded view of the bow shocks and possible driving jets. Contours show highly blue-shifted emission of [O III] (cyan, centered on -70 km s^{-1}) and [N II] (yellow, centered on -50 km s^{-1} , and white, centered on -35 km s^{-1}), derived from multiple longslit spectra (Doi et al. 2004 as recalibrated in spectral atlas of García-Díaz et al. 2008). Mean velocities with respect to the Orion Nebular Cluster of particular features related to the HH objects are indicated by arrows. (b) Location of HH 204 with respect to the inner Orion Nebula. The intensity of the image comes from the [N II] *HST* WFPC2 observations, but colorized according to the velocity of the slow-moving nebular gas (within about 30 km s^{-1} of the systemic velocity) as derived from the longslit spectra, see color key on figure. (c) Highly blue-shifted [O III] emission for a field of view similar to that of panel b. (d) As panel c but for highly blue-shifted [N II] emission. Two candidate stellar sources along the back-projection of the PA108 flow are indicated by white circles (see discussion in text). (e) Near-infrared HAWK-I imaging of the region outlined by a yellow dashed box in panel d in the $2.12 \mu\text{m}$ H_2 line (Kissler-Patig et al. 2008), showing an emission filament that may be associated with HH 204.

In Figure 22b we show the back projection of all three of these flows into the core of the nebula, assuming an uncertainty of $\pm 10^\circ$ for the PA108 flow and $\pm 5^\circ$ for the other two. The PA118 flow is consistent with an origin in the Orion S star forming region, as has been remarked many times previously (O'Dell et al. 1997b; Rosado et al. 2002; O'Dell & Doi 2003). However, neither of the other flows are consistent with an origin in that region, unless the flow has suffered a relatively large-angle deviation. The back-projection of the PA108 falls significantly to the south of the main Orion S region in an area with no convincing candidates for the driving source (see above discussion of the possible H₂ jet). The back projection of the PA140 flow intersects the Trapezium stars in the very center of the nebula, which raises the possibility that the source may be a proplyd, which are highly concentrated in that region.

9. DISCUSSION

The high spectral resolution of our data ($\lambda/\Delta\lambda \approx 6.5 \text{ km s}^{-1}$) allows to identify and properly separate 3 kinematical components of ionized gas: the Diffuse Blue Layer (DBL), the emission of the Orion Nebula and HH 204. In the following we will discuss in detail the results concerning each of these components.

9.1. The Diffuse Blue Layer

The component designated as the DBL was firstly reported by Deharveng (1973), although it has been little studied, since high spectral resolution is required to separate its emission from that of the Orion Nebula. García-Díaz & Henney (2007) analyzed the velocity structure of the Orion Nebula through the emission of [OI], [SII] and [SIII] lines, using echelle spectroscopy. They detected the emission of the [SII] doublet from the DBL, estimating a density of $\sim 400 \text{ cm}^{-3}$, which is in complete agreement with our estimates. These authors did not detect the emission of [OI] or [S III] in this component, although the emission of other low ionization ions such as [OII] and [N II] was detected in previous works (Jones 1992; Henney & O'Dell 1999). These limited spectroscopical evidences lead to interpret the DBL as composed by fully ionized gas, whose ionizing radiation field was rather soft, probably coming from θ^2 Ori A. We have detected all these lines along with [OI] and [SIII] ones in the spectrum of this component extracted from cut 2 (see upper and middle panel of Fig. 23). These emissions were also reported by O'Dell (2018) in a later re-analysis of the atlas of lines of García-Díaz & Henney (2007). In addition, we detect a weak [O III] emission, indicative of the presence of gas with a high degree of ionization as it is shown in the lower panel of Fig. 23.

Through observations of HI 21-cm emission, van der Werf et al. (2013) determined the existence of several HI velocity components in the Orion Nebula. At the southeast, in the area where the DBL is located, these authors identified a blueshifted component named “D”, interpreted as an expanding shell centered on θ^2 Ori B, which is consistent with a scenario where this star ionizes the DBL. The observed [OI] emission is consistent with the presence of an ionization front (IF) in this nebular feature. However, with the new information provided by the ionic abundances of the DBL – estimated for the first time in this work – the simple model where the gas is photoionized exclusively by θ^2 Ori B may not be correct. Although small, the contribution of O²⁺ to the total abundance is not negligible, being around 10%. On the other hand, assuming that the DBL should have a chemical composition similar to the Orion Nebula, this implies that the estimated N⁺ abundance is approximately 75% of the total nitrogen abundance, therefore N²⁺ should be present in this component. Since θ^2 Ori B is a B0.7V star (Simón-Díaz 2010), we do not expect such a star to emit a number of photons capable of maintaining a significant proportion of highly ionized ions. This is reinforced by the spectroscopical results of Galactic H II regions ionized by B-type stars such as Sh 2-32, Sh 2-47, Sh 2-82, Sh 2-175, Sh 2-219, Sh 2-270, Sh 2-285, Sh 2-297 and IC 5146 (García-Rojas et al. 2014; Esteban & García-Rojas 2018; Arellano-Córdova et al. 2021). In all these regions, nitrogen is only once ionized and the contribution of O²⁺ to the total oxygen is lower than 2%, with the exception of the faint Sh 2-47, although the O²⁺ abundance determination in this object is very uncertain.

As we can see in the discussion above, the spectroscopical properties of the DBL suggest some ionization by radiation leakage from the Orion Nebula. Simón-Díaz et al. (2011) found abnormal emission of CELs of high-ionized species (mainly [O III]) in the external zones of M 43, an H II region ionized by a B0.5V star located at the northeast of the Orion Nebula. As those authors demonstrate, the spectral properties of this abnormal emission is consistent with contamination by scattered light from the Huygens Region. In our case, we can discard the scattered nature of the emission of high-ionized ions in the DBL because (i) it has the same velocity as the lines of low-ionization ions, (ii) we do not detect anomalies in the Balmer decrement of the spectrum of the DBL, that would be a signature of the presence of scattered emission (see Simón-Díaz et al. 2011). Further observations with longer exposure time, similar spectral resolution and covering different areas of the Orion Neb-

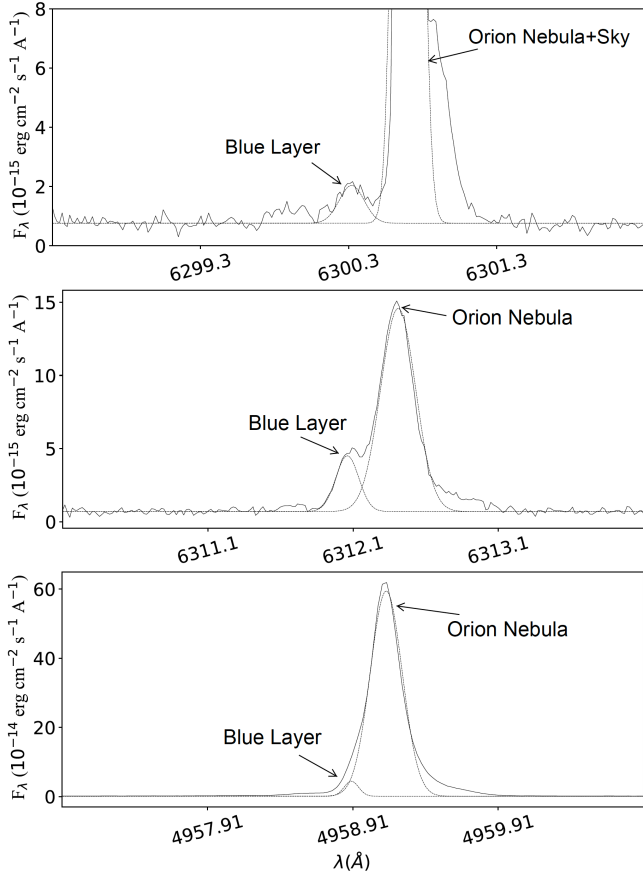


Figure 23: Spectrum of cut 2 showing the emission of [OI] $\lambda 6300$ (upper panel), [S III] $\lambda 6312$ (middle panel) and [O III] $\lambda 4959$ (lower panel) of the DBL and the Orion Nebula.

ula would shed more light on the extension and physical, chemical and geometrical properties of the DBL.

9.2. The Nebular Component

There are notable differences in the degree of ionization and physical conditions of the gas of the nebular component studied in this work and in Paper I. The degree of ionization in the area of the Orion Nebula observed in this paper is $O^{2+}/O = 0.42 \pm 0.04$ and ~ 0.8 in that observed in Paper I. This is an expected behavior considering the different distances of both areas with respect to the main ionizing star. The density in the nebular component in the direction of HH 204 is $n_e = 1440 \pm 170 \text{ cm}^{-3}$, significantly lower than the values of $n_e \sim 6000 \text{ cm}^{-3}$ obtained around HH 529 II and III in Paper I. This result, is again consistent with the more external position of HH 204 with respect to θ^1 Ori C and the centre of a blister-shaped nebula. There is a remarkable consistency between the $T_e([O\text{ III}])$ and $T_e([N\text{ II}])$ values we obtain in this paper with the predictions of the radial distribution of those

quantities given in eqs. 4 and 5 of Mesa-Delgado et al. (2008), confirming that the temperature decreases linearly with the radial distance from θ^1 Ori C in the Orion Nebula.

As expected, the total abundances of O, N, S and Cl shown in Table 7 are in good agreement with those included in Table 11 of Paper I. However, the abundances of Ne and Ar are somewhat different because the use of different ICFs to estimate the contribution of unseen Ar^+ and Ne^+ , which is larger due to the lower degree of ionization of the nebular component in the direction to HH 204. A similar situation occurs with the C abundance, which requires large corrections to estimate the important contribution of C^+ . Although the total abundance of O = 8.42 ± 0.04 we obtain using CELs is entirely consistent with the value of O = 8.46 ± 0.03 derived in Paper I, both are somewhat lower than the value of O = 8.51 ± 0.03 obtained by Esteban et al. (2004) and Mesa-Delgado et al. (2009) in two different areas of the Orion Nebula. It is important to note that this difference seems to be correlated with the abundance discrepancy factor (ADF) of O^{2+} estimated in each observed area. The values of ADF(O^{2+}) are 0.36, 0.20, 0.13 and 0.11 for the nebular component of this work, Paper I, Esteban et al. (2004) and Mesa-Delgado et al. (2009), respectively. If we add the difference between the measured ADF(O^{2+}) and 0.12 – the average value found by Esteban et al. (2004) and Mesa-Delgado et al. (2009) – to the O^{2+} abundance determined from CELs in this work and Paper I, we obtain O = 8.53 ± 0.03 for both, matching the values obtained by Esteban et al. (2004) and Mesa-Delgado et al. (2009) within the uncertainties. Moreover, if we add the measured ADF(O^{2+}) to the O^{2+} abundance from CELs, the four aforementioned determinations of the total oxygen abundance in Orion Nebula components converge to the same value of ~ 8.6 . In any case, there are other explanations for the different O abundances obtained in different zones of the nebula. One can be related to a different depletion factor of O onto dust grains. This element may be trapped in the form of oxides, pyroxenes or olivines, compounds that would include atoms of metals such as Fe. However, the total abundance of Fe does not differ substantially between the aforementioned four zones of the the Orion Nebula and, unfortunately, the relatively large uncertainties associated with the Fe/H ratio do not permit to trace differences in the depletion factors.

9.3. HH 204

Our spectroscopic observations allow the analysis of the physical conditions and ionic abundances of HH 204 with unprecedented detail. The results show that the

gas is compressed as it approaches the bowshock, increasing its density. On the other hand, $T_e(\text{[N II]})$ and $T_e(\text{[S III]})$ remain unaltered by the shock, being consistent with the expected values for a gas in photoionization equilibrium, while $T_e(\text{[O III]})$ seems to be altered, reaching the maximum values at the bowshock and decreasing when moving away – towards the interior of the jet – from this point until its value stabilizes to temperatures more similar to those given by the rest of diagnostics. Due to the increase in density when approaching the bowshock and in the distance to θ^1 Ori C, the degree of ionization of the gas – measured as the O^{2+}/O ratio – drops almost to zero. In fact, the density increase is enough to trap an ionization front, that becomes evident through the detection of emission lines of neutral elements such as [OI] and [NI]. This aspect deserves further discussion. In previous studies, the detection of lines of neutral species has been interpreted as product of the interaction of HH 204 with neutral material, such as that found in the Orion's Veil ([O'Dell et al. 1997b,a; Takami et al. 2002](#)). However, there are several arguments against this scenario and in favor of the trapped ionization front. (i) The spatial distribution of the [OI] emission, shown in Fig. 2, is more concentrated than that of [OII] or [OIII], located at the southeast of HH 204, in the opposite direction to θ^1 Ori C, consistent with a zone shielded from the ionizing radiation. (ii) As we discussed in Sec. 5.4, the isotopic shift of the deuterium lines with respect to hydrogen ones coincides with the theoretical one in HH 204. Since this radiation arises from areas slightly beyond the ionization front, this also implies that HH 204 should also contain a trapped ionization front. Finally, (iii) the combination of the tangential and radial motions of HH 204 allows to know its 3D-trajectory. From its apparent distance to Orion-S (its likely origin), [Doi et al. \(2004\)](#) estimate that HH 204 has moved ~ 0.15 pc radially towards the observer. Although [van der Werf et al. \(2013\)](#) argued that the Orion Veil lays ~ 0.3 pc apart from Orion-S, [Abel et al. \(2016\)](#) established that the distance must be significantly larger and therefore a direct interaction between HH 204 and the Veil is unlikely. If those distance estimations are correct, HH 204 would be located within the main ionized gas volume of the Orion Nebula or interacting with the Nearer Ionized Layer (NIL, see [Abel et al. 2019; O'Dell et al. 2020](#)).

In HH 204, the O^+ abundances calculated with RLs and CELs match. Since in this object practically all the oxygen is once ionized, this implies that HH 204 – contrary to what is usually found in ionized nebulae – does not show an ADF in both, O^+ and O abundances. In Sec. 5.2 we discussed 3 phenomena that may be the

cause of the ADF and that in HH 204 should presumably have a negligible impact: (i) temperature fluctuations, (ii) starlight fluorescence and (iii) chemical or density inhomogeneities. The consistency of the O abundances determined from RLs and CELs in HH 204 suggests that its true value should be ~ 8.6 , slightly lower than the recommended solar O abundance (8.73 ± 0.07 , [Lodders 2019](#)).

In Table 8 we compile the O abundances obtained in all chemical abundance studies of the Orion Nebula based on deep echelle spectroscopy taken with UVES. A note of caution should be given because any comparison among the abundances of the different zones must consider that a fraction of O may be depleted onto dust grains, and this may be different along the nebula. For example, [Mesa-Delgado et al. \(2009\)](#) estimated such fraction to be ~ 0.12 dex. However, it can be lowered by destruction of dust grains due to the passage of shocks, specially in the HH objects. We recommend to consider a maximum extra uncertainty of ~ 0.1 dex to any given O abundance to include unaccounted depletion variations.

If we assume that the O abundances based on RLs are the true ones in all objects, we have some issues to consider. HH 529 II and III and other zones of the Orion Nebula show larger O/H ratios than the rest. In Paper I we discuss the possibility of having a slight overmetallicity in HH 529 II and III, due to the entrainment of material from the accretion disk of the stellar source of the jets. On the other hand, the O abundances based on RLs found in the nebular components studied in Paper I and [Esteban et al. \(2004\)](#) are also somewhat higher than what is found in HH 204. These differences may have different explanations in each case, apart from the previously mentioned dust depletion variations.

If we assume that the O abundances based on CELs are the true ones, we could reconcile all the observed values simply by considering different proportions of O depletion onto dust grains in addition to small contributions from other phenomena as, for example, temperature fluctuations. In this context, if we assume that half of the difference between ~ 8.6 – considering that the O abundance obtained in HH 204 is the true one of the Orion Nebula – and the O abundance based on CELs obtained by [Esteban et al. \(2004\)](#) is due to dust depletion and the rest to temperature fluctuations, this would be compatible with $t^2 \sim 0.008$, a value considerable smaller than the $t^2 \sim 0.022$ necessary to match the O abundances from RLs obtained in the same spectrum. In this case, the important question is why the RLs are giving higher O abundances in all cases except HH 204. An important difference between the determination of O abundance in HH 204 and the other zones or objects in-

cluded in Table 8 is that, in HH 204, the contribution of O^{2+} to the total abundance is negligible. It is important to say that Mesa-Delgado et al. (2009) also obtained an ADF(O^+) equal to zero in both, HH 202 S and the nebular component. However, the contribution of O^{++} is important in those spectra and their ADF(O^{++}) are not zero. This result suggests that the AD may be related to unaccounted effects affecting the intensity of O II RLs, although it is still premature to point out any conclusion in this regard. We plan to explore this important issue further in future papers of this series.

The low ionization degree of HH 204 is an advantage for determining the abundance of certain elements. In areas close to the bowshock, where the ionization degree drops to practically zero, we can obtain the total abundance of N, S, Cl, Fe and Ni without the use of an ICF, simply adding the ionic abundances determined from our optical spectrum. This makes it possible to eliminate the generally most important source of uncertainty and thus obtain very precise abundances, which can be used as representative of the Orion Nebula.

From Table 7, it is clear that the Fe abundance in HH 204 is higher than in the other components due to dust destruction in the bowshock. Following the same procedure as in Paper I, comparing the observed Fe/O values in HH 204 and the nebular component with the expected solar value (Lodders 2019), we estimate that $\sim 6\%$ of the total Fe is in the gaseous phase in the nebular component, while this fraction goes up to 21% in HH 204, representing an increase of a factor 3.5. A similar factor may be assumed for Ni, considering the results of Sec. 4.3 that show similar depletion patterns for Fe and Ni.

Based in the study of the sub-arcsecond *HST* imaging, we found an increase in the [O III]/H α emission at the edge of the geometry of HH 204. The width of this layer varies at different spatial positions, being minimal near the bowshock, where the density is higher. This [O III]/H α peak emission is originated in the cooling zone that is formed after the shock passing. We find three possible driving jets flowing towards the HH 203/HH 204 region. These have position angles of 108°, 118° and 140° (PA108, PA118 and PA140). The first one seems to feed HH 204, while the last two seem to give rise to HH 203, being this object apparently a superposition of two unrelated bowshocks. The possible connection between both HH objects is still not confirmed but it is quite clear that the gas flow of PA118 is not driving HH 204. The back projection of these flows are consistent with an origin in the south of Orion S, the main body of Orion S and close to the Trapezium stars for PA108, PA118 and PA140, respectively.

9.4. On the presence of high-density inclusions

Last but not least we want to discuss the influence of the presence of a high-density component in the spectrum of a photoionized region when it is not detected in the observations. We have studied this scenario in Sec. 7 adding the nebular emission from the Orion Nebula, the DBL and HH 204, which would be obtained when observing with a velocity resolution lower than ~ 54 km s $^{-1}$ or $R \approx 5550$. In this case, the classical density diagnostics such as $I(\lambda 3726)/I(\lambda 3729)$ ([O II]), $I(\lambda 6716)/I(\lambda 6731)$ ([S II]) and $I(\lambda 5518)/I(\lambda 5538)$ ([Cl III]) are not sensitive to the high density of HH 204. In the case of the first two diagnostics, the resulting density is biased towards the values of the Orion Nebula and the DBL. Although the [Cl III] is sensitive at somewhat higher densities, it traces specially the conditions of the Orion Nebula because the higher ionization degree of [Cl III]. Incorrectly lower density values determined with these diagnostics lead to an overestimate of T_e ([N II]) and underestimate of abundances of some elements. In the case of O^+ , the underestimate would be ~ 0.2 dex (see Sec. 7), producing a similar impact on the total O abundance, as O^+ is the dominant ion. However, the problem affects indirectly to other elements which total abundance is based on highly ionized ions through the ICFs. This is because they depend on the degree of ionization, parameterized by $O^{2+}/(O^{2+}+O^+)$. The impact of high-density inclusions or components onto the abundances will depend on their contribution to the integrated volume, degree of ionization and density.

Previous studies of the area of HH 204 – all based on lower spectral resolution spectroscopy – reported localized peaks of T_e ([N II]) (Mesa-Delgado et al. 2008; Núñez-Díaz et al. 2012; O’Dell et al. 2017a), which were interpreted as the product of shock heating. The results presented in Sec. 5 demonstrate that this interpretation is not correct. The apparent peaks of T_e ([N II]) are artifacts produced by the use of n_e values that are below the true ones. T_e ([O III]) does not show such peaks due to the very low ionization degree of HH 204 and the higher critical densities of [O III] lines. In Table 3 we can see that, for HH 204, even the classical density diagnostics give values consistent with those obtained from the ratio of [Fe III] lines. This is because HH 204, due to its orientation and the spectral resolution of the observations, can be interpreted basically as a single slab of high-density gas. This would be different in the case of an HH object moving directly towards us and observed with low resolution spectroscopy. We would most likely have a density gradient in the line of sight, because it will cross the compressed gas at the bowshock and the

Table 8: Oxygen abundances in the Orion Nebula based on UVES spectroscopy.

Region	RLs			CELS			Reference
	O ⁺	O ²⁺	O	O ⁺	O ²⁺	O	
Orion Nebula	8.15 ± 0.13	8.57 ± 0.01	8.71 ± 0.03	7.76 ± 0.15	8.43 ± 0.01	8.51 ± 0.03	Esteban et al. (2004)
	8.01 ± 0.12	8.46 ± 0.03	8.59 ± 0.05	8.00 ± 0.06	8.35 ± 0.03	8.51 ± 0.03	Mesa-Delgado et al. (2009)
	8.25 ± 0.06	8.52 ± 0.02	8.70 ± 0.03	7.83 ± 0.05	8.35 ± 0.03	8.46 ± 0.03	Méndez-Delgado et al. (2021)
	-	8.40 ± 0.03	8.60 ± 0.03*	8.18 ± 0.06	8.04 ± 0.02	8.42 ± 0.04	This work
HH 202 S	8.25 ± 0.16	8.44 ± 0.03	8.65 ± 0.05	8.29 ± 0.06	8.08 ± 0.03	8.50 ± 0.04	Mesa-Delgado et al. (2009)
HH 529 II	< 7.91	8.83 ± 0.07	8.83 ± 0.07	7.36 ± 0.12	8.54 ± 0.03	8.57 ± 0.03	Méndez-Delgado et al. (2021)
HH 529 III	< 7.95	8.84 ± 0.09	8.84 ± 0.09	7.51 ± 0.22	8.48 ± 0.03	8.53 ± 0.03	Méndez-Delgado et al. (2021)
HH 204	8.57 ± 0.03	< 7.54	8.57 ± 0.03	8.62 ± 0.05	6.34 ± 0.02	8.62 ± 0.05	This Work

NOTE—Abundances in units of $12 + \log(X^{n+}/H^+)$ or $12 + \log(X/H)$.

* Using the O⁺ abundance based on CELs.

less denser material traveling behind along the jet axis. In situations like this, a way to detect the presence of high-density inclusions – as HH objects – can be the use of the $I([Fe\,III]\lambda 4658)/I([Fe\,III]\lambda 4702)$ ratio as a density diagnostic. Considering the used atomic data for Fe²⁺, this ratio is practically insensitive at densities lower than $\sim 10^3$ cm⁻³, while its critical density is above $\sim 10^6$ cm⁻³. In the case of a gas inclusion with density of around or larger than $\sim 10^4$ cm⁻³ immersed in a region with an overall density of $10^2 - 10^3$ cm⁻³, this diagnostic will be biased to the higher density component, while classical ones will be biased in the opposite direction. A significant discrepancy between the [Fe III] diagnostic and classical ones in a region of apparently low n_e may serve as an indicator of this kind of situations. However, factors such as the degree of ionization of the gas and the relative volume occupied by each mixed component can mask density inhomogeneities. It is advisable to analyze each available density diagnostic even if they are discrepant since such discrepancies may be real.

10. CONCLUSIONS

We have studied the physical conditions – n_e , T_e –, chemical composition and other properties of the photoionized Herbig-Haro object HH 204, as well as the Diffuse Blue Layer and the Orion Nebula emission located in the same line of sight through deep high-spectral resolution UVES spectroscopy and *HST* imaging.

We have analyzed the distribution of the physical conditions of HH 204 along the slit with sub-arcsecond spatial resolution. We find an steady increase of n_e from ~ 10000 cm⁻³ at ~ 13 mpc behind the bowshock to ~ 20000 cm⁻³ close to it. On the other hand, $T_e([N\,II])$ and $T_e([S\,III])$ remain both rather constant, showing

that the low-intermediate ionization degree gas is in photoionization equilibrium. However, $T_e([O\,III])$ seems to be affected by shock heating in the area closest to the bowshock. Based on the observed distribution of $T_e([O\,III])$ and assuming the most likely 3D geometry of the observed area of HH 204, we perform what we think may be the most plausible estimate of the Peimbert's t^2 representative of the integrated gas volume of a nebular object.

We estimate that around $\sim 99\%$ of the gas in the observed area of HH 204 is composed by low and intermediate ionization degree ions. Based on the intensity of CELs, we determine the ionic abundances of O⁺, O²⁺, N⁺, Ne²⁺, S⁺, S²⁺, Cl⁺, Cl²⁺, Ar²⁺, Fe⁺, Fe²⁺, Ni⁺, Ni²⁺, Ca⁺ and Cr⁺. We also calculate the ionic abundances of He⁺, O⁺ and C²⁺ from the intensity of RLs. In HH 204, we find no difference when determining the O⁺ abundance using CELs or RLs. Since practically all O is O⁺ in this object, we can say that the abundance discrepancy (AD) is virtually zero for HH 204, contrary with what is found in essentially all ionized nebulae. Both, CELs and RLs provide an O abundance of $\sim 8.60 \pm 0.05$, slightly lower than the solar value of O = 8.73 ± 0.07 recommended by Lodders (2019), but consistent with many other independent determinations in the Orion Nebula.

Due to the low degree of ionization of HH 204, we can derive the O, N, S, Cl, Fe and Ni abundances without ICFs. In principle, those abundances should be representative of the Orion Nebula as well. Furthermore, we find that the ionic abundances of Fe and Ni show similar ionization and depletion patterns. Due to the destruction of dust grains containing Fe and Ni atoms at the bowshock, their abundances are a factor 3.5 higher than in the Orion Nebula. We also found direct evidences of

the presence of an ionization front trapped in HH 204 such as the detection of deuterium lines produced by non-ionizing far-UV photons.

Taking advantage of the high spatial resolution of the *HST* imaging, we report the presence of a narrow high [O III]/H α zone produced by the cooling process after the shock passage. We propose three possible driving jets of HH 203 and HH 204 at PA108, PA118 and PA140. The first one, whose back projection originates in the south of the Orion-S, is a strong candidate to feed HH 204 while the last two seem to give rise to HH 203, which is apparently a superposition of two unrelated bowshocks. We do not find any conclusive connection between both HH objects.

Our observations permit to separate and analyze the spectrum of the Diffuse Blue Layer, an ionized gas component with a radial velocity different from that of the Orion Nebula and HH 204. We have estimated its physical conditions – its T_e for the first time –, revealing that it has a density lower than the Orion Nebula. We have calculated its chemical composition for the first time. This component seems to be ionized by leaking photons from the Orion Nebula.

Our analysis of the spectrum of the kinematical component corresponding to the Orion Nebula reveals a lower ionization degree and n_e with respect to the results of Paper I. This comparison also indicates that T_e in the Orion Nebula decrease with the radial distance from θ^1 Ori C. The chemical composition of the nebular component is similar to what found in Paper I, however, there seems to be a slightly lower O abundance (less than 0.04 dex), perhaps related to different depletion factors onto dust grains of this element.

We carry out the exercise of simulating a spectrum with lower spectral and spatial resolution, where the spectra of the different kinematical components are mixed. We find that the analysis of this integrated spec-

trum can lead to wrong physical conditions and chemical abundances. For example, the estimation of n_e by averaging $n_e(\text{[O II]})$, $n_e(\text{[S II]})$ and $n_e(\text{[Cl III]})$ underestimates the real density, resulting in an overestimation of the temperature of the low ionization ions, which constitute an important fraction of the gas in HH 204, the dominant component of the integrated spectrum. This fact leads to underestimate the abundances and to obtain a wrong average ionization degree, the parameter on most ICF schemes are based. Therefore, the determination of the chemical abundances would be wrong in practically all elements. Indicators of density such as $I(\text{[Fe III]} \lambda 4658)/I(\text{[Fe III]} \lambda 4702)$ may be used to detect the presence of high density clumps associated to HH objects or shocks.

ACKNOWLEDGEMENTS

This work is based on observations collected at the European Southern Observatory, Chile, proposal number ESO 092.C-0323(A). We acknowledge support from the Agencia Estatal de Investigación del Ministerio de Ciencia e Innovación (AEI-MCINN) under grant *Especroscopía de campo integral de regiones H II locales. Modelos para el estudio de regiones H II extragalácticas* with reference 10.13039/501100011033. JG-R acknowledges support from Advanced Fellowships from the Severo Ochoa excellence programs SEV-2015-0548 and CEX2019-000920-S. JEM-D thanks the support of the Instituto de Astrofísica de Canarias under the Astrophysicist Resident Program and acknowledges support from the Mexican CONACyT (grant CVU 602402). The authors acknowledge support under grant P/308614 financed by funds transferred from the Spanish Ministry of Science, Innovation and Universities, charged to the General State Budgets and with funds transferred from the General Budgets of the Autonomous Community of the Canary Islands by the MCIIU.

REFERENCES

- Abel, N. P., Ferland, G. J., & O'Dell, C. R. 2019, ApJ, 881, 130, doi: [10.3847/1538-4357/ab2a6e](https://doi.org/10.3847/1538-4357/ab2a6e)
- Abel, N. P., Ferland, G. J., O'Dell, C. R., & Troland, T. H. 2016, ApJ, 819, 136, doi: [10.3847/0004-637X/819/2/136](https://doi.org/10.3847/0004-637X/819/2/136)
- Arellano-Córdova, K. Z., Esteban, C., García-Rojas, J., & Méndez-Delgado, J. E. 2020, MNRAS, 496, 1051, doi: [10.1093/mnras/staa1523](https://doi.org/10.1093/mnras/staa1523)
- . 2021, MNRAS, 502, 225, doi: [10.1093/mnras/staa3903](https://doi.org/10.1093/mnras/staa3903)
- Badnell, N. R., & Ballance, C. P. 2014, ApJ, 785, 99, doi: [10.1088/0004-637X/785/2/99](https://doi.org/10.1088/0004-637X/785/2/99)
- Baldwin, J. A., Crotts, A., Dufour, R. J., et al. 1996, ApJL, 468, L115, doi: [10.1086/310245](https://doi.org/10.1086/310245)
- Bautista, M. A. 2001, A&A, 365, 268, doi: [10.1051/0004-6361:20000032](https://doi.org/10.1051/0004-6361:20000032)
- . 2004, A&A, 420, 763, doi: [10.1051/0004-6361:20035719](https://doi.org/10.1051/0004-6361:20035719)
- Bautista, M. A., Ballance, C. P., & Quinet, P. 2010, ApJL, 718, L189, doi: [10.1088/2041-8205/718/2/L189](https://doi.org/10.1088/2041-8205/718/2/L189)
- Bautista, M. A., Fivet, V., Ballance, C., et al. 2015, ApJ, 808, 174, doi: [10.1088/0004-637X/808/2/174](https://doi.org/10.1088/0004-637X/808/2/174)
- Bautista, M. A., Peng, J., & Pradhan, A. K. 1996, ApJ, 460, 372, doi: [10.1086/176976](https://doi.org/10.1086/176976)
- Bautista, M. A., & Pradhan, A. K. 1998, ApJ, 492, 650, doi: [10.1086/305061](https://doi.org/10.1086/305061)

- Bhatia, A. K., & Kastner, S. O. 1995, *ApJS*, 96, 325, doi: [10.1086/192121](https://doi.org/10.1086/192121)
- Binder, B. A., & Povich, M. S. 2018, *ApJ*, 864, 136, doi: [10.3847/1538-4357/aad7b2](https://doi.org/10.3847/1538-4357/aad7b2)
- Blagrave, K. P. M., Martin, P. G., & Baldwin, J. A. 2006, *ApJ*, 644, 1006, doi: [10.1086/503830](https://doi.org/10.1086/503830)
- Blagrave, K. P. M., Martin, P. G., Rubin, R. H., et al. 2007, *ApJ*, 655, 299, doi: [10.1086/510151](https://doi.org/10.1086/510151)
- Butler, K., & Zeippen, C. J. 1989, *A&A*, 208, 337
- Cantó, J., Goudis, C., Johnson, P. G., & Meaburn, J. 1980, *A&A*, 85, 128
- Cox, D. P., & Raymond, J. C. 1985, *ApJ*, 298, 651, doi: [10.1086/163649](https://doi.org/10.1086/163649)
- Davey, A. R., Storey, P. J., & Kisielius, R. 2000, *A&AS*, 142, 85, doi: [10.1051/aas:2000139](https://doi.org/10.1051/aas:2000139)
- Deharveng, L. 1973, *A&A*, 29, 341
- D’Odorico, S., Cristiani, S., Dekker, H., et al. 2000, Society of Photo-Optical Instrumentation Engineers (SPIE) Conference Series, Vol. 4005, Performance of UVES, the echelle spectrograph for the ESO VLT and highlights of the first observations of stars and quasars, ed. J. Bergeron, 121–130, doi: [10.1117/12.390133](https://doi.org/10.1117/12.390133)
- Doi, T., O’Dell, C. R., & Hartigan, P. 2002, *AJ*, 124, 445, doi: [10.1086/341044](https://doi.org/10.1086/341044)
- . 2004, *AJ*, 127, 3456, doi: [10.1086/386351](https://doi.org/10.1086/386351)
- Escalante, V., Morisset, C., & Georgiev, L. 2012, *MNRAS*, 426, 2318, doi: [10.1111/j.1365-2966.2012.21862.x](https://doi.org/10.1111/j.1365-2966.2012.21862.x)
- Esteban, C., & García-Rojas, J. 2018, *MNRAS*, 478, 2315, doi: [10.1093/mnras/sty1168](https://doi.org/10.1093/mnras/sty1168)
- Esteban, C., García-Rojas, J., & Pérez-Mesa, V. 2015, *MNRAS*, 452, 1553, doi: [10.1093/mnras/stv1367](https://doi.org/10.1093/mnras/stv1367)
- Esteban, C., Peimbert, M., García-Rojas, J., et al. 2004, *MNRAS*, 355, 229, doi: [10.1111/j.1365-2966.2004.08313.x](https://doi.org/10.1111/j.1365-2966.2004.08313.x)
- Esteban, C., Peimbert, M., Torres-Peimbert, S., & Escalante, V. 1998, *MNRAS*, 295, 401, doi: [10.1046/j.1365-8711.1998.01335.x](https://doi.org/10.1046/j.1365-8711.1998.01335.x)
- Fritzsche, S., Fricke, B., Geschke, D., Heitmann, A., & Sienkiewicz, J. E. 1999, *ApJ*, 518, 994, doi: [10.1086/307328](https://doi.org/10.1086/307328)
- Froese Fischer, C., Rubin, R. H., & Rodríguez, M. 2008, *MNRAS*, 391, 1828, doi: [10.1111/j.1365-2966.2008.13997.x](https://doi.org/10.1111/j.1365-2966.2008.13997.x)
- Froese Fischer, C., & Tachiev, G. 2004, *Atomic Data and Nuclear Data Tables*, 87, 1, doi: [10.1016/j.adt.2004.02.001](https://doi.org/10.1016/j.adt.2004.02.001)
- Gaia Collaboration, Brown, A. G. A., Vallenari, A., et al. 2018, *A&A*, 616, A1, doi: [10.1051/0004-6361/201833051](https://doi.org/10.1051/0004-6361/201833051)
- Galavis, M. E., Mendoza, C., & Zeippen, C. J. 1995, *A&AS*, 111, 347
- García-Díaz, M. T., & Henney, W. J. 2007, *AJ*, 133, 952, doi: [10.1086/510621](https://doi.org/10.1086/510621)
- García-Díaz, M. T., Henney, W. J., López, J. A., & Doi, T. 2008, *RMxAA*, 44, 181. <https://arxiv.org/abs/0802.0518>
- García-Rojas, J., & Esteban, C. 2007, *ApJ*, 670, 457, doi: [10.1086/521871](https://doi.org/10.1086/521871)
- García-Rojas, J., Esteban, C., Peimbert, A., et al. 2005, *MNRAS*, 362, 301, doi: [10.1111/j.1365-2966.2005.09302.x](https://doi.org/10.1111/j.1365-2966.2005.09302.x)
- . 2007, *RMxAA*, 43, 3. <https://arxiv.org/abs/astro-ph/0610065>
- García-Rojas, J., Esteban, C., Peimbert, M., et al. 2006, *MNRAS*, 368, 253, doi: [10.1111/j.1365-2966.2006.10105.x](https://doi.org/10.1111/j.1365-2966.2006.10105.x)
- García-Rojas, J., Simón-Díaz, S., & Esteban, C. 2014, *A&A*, 571, A93, doi: [10.1051/0004-6361/201424660](https://doi.org/10.1051/0004-6361/201424660)
- Grieve, M. F. R., Ramsbottom, C. A., Hudson, C. E., & Keenan, F. P. 2014, *ApJ*, 780, 110, doi: [10.1088/0004-637X/780/1/110](https://doi.org/10.1088/0004-637X/780/1/110)
- Hartigan, P., Raymond, J., & Hartmann, L. 1987, *ApJ*, 316, 323, doi: [10.1086/165204](https://doi.org/10.1086/165204)
- Hébrard, G., Péquignot, D., Vidal-Madjar, A., Walsh, J. R., & Ferlet, R. 2000a, *A&A*, 354, L79. <https://arxiv.org/abs/astro-ph/0002141>
- Hébrard, G., Péquignot, D., Walsh, J. R., Vidal-Madjar, A., & Ferlet, R. 2000b, *A&A*, 364, L31. <https://arxiv.org/abs/astro-ph/0008420>
- Henney, W. J., & O’Dell, C. R. 1999, *AJ*, 118, 2350, doi: [10.1086/301087](https://doi.org/10.1086/301087)
- Henney, W. J., O’Dell, C. R., Zapata, L. A., et al. 2007, *AJ*, 133, 2192, doi: [10.1086/513074](https://doi.org/10.1086/513074)
- Johansson, S., Zethson, T., Hartman, H., et al. 2000, *A&A*, 361, 977
- Jones, M. R. 1992, PhD thesis, RICE UNIVERSITY.
- Kaufman, V., & Sugar, J. 1986, *Journal of Physical and Chemical Reference Data*, 15, 321, doi: [10.1063/1.555775](https://doi.org/10.1063/1.555775)
- Kisielius, R., Storey, P. J., Ferland, G. J., & Keenan, F. P. 2009, *MNRAS*, 397, 903, doi: [10.1111/j.1365-2966.2009.14989.x](https://doi.org/10.1111/j.1365-2966.2009.14989.x)
- Kissler-Patig, M., Pirard, J. F., Casali, M., et al. 2008, *A&A*, 491, 941, doi: [10.1051/0004-6361:200809910](https://doi.org/10.1051/0004-6361:200809910)
- Laha, S., Tyndall, N. B., Keenan, F. P., et al. 2017, *ApJ*, 841, 3, doi: [10.3847/1538-4357/aa7071](https://doi.org/10.3847/1538-4357/aa7071)
- Liu, X. W., Luo, S. G., Barlow, M. J., Danziger, I. J., & Storey, P. J. 2001, *MNRAS*, 327, 141, doi: [10.1046/j.1365-8711.2001.04676.x](https://doi.org/10.1046/j.1365-8711.2001.04676.x)
- Lodders, K. 2019, arXiv e-prints, arXiv:1912.00844. <https://arxiv.org/abs/1912.00844>
- Lucy, L. B. 1995, *A&A*, 294, 555
- Luridiana, V., Morisset, C., & Shaw, R. A. 2015, *A&A*, 573, A42, doi: [10.1051/0004-6361/201323152](https://doi.org/10.1051/0004-6361/201323152)
- McLaughlin, B. M., Lee, T.-G., Ludlow, J. A., et al. 2011, *Journal of Physics B Atomic Molecular Physics*, 44, 175206, doi: [10.1088/0953-4075/44/17/175206](https://doi.org/10.1088/0953-4075/44/17/175206)

- Meléndez, M., Bautista, M. A., & Badnell, N. R. 2007, *A&A*, 469, 1203, doi: [10.1051/0004-6361:20077262](https://doi.org/10.1051/0004-6361:20077262)
- Méndez-Delgado, J. E., Esteban, C., García-Rojas, J., et al. 2021, *MNRAS*, 502, 1703, doi: [10.1093/mnras/stab068](https://doi.org/10.1093/mnras/stab068)
- Mendoza, C. 1983, in IAU Symposium, Vol. 103, Planetary Nebulae, ed. L. H. Aller, 143–172
- Mendoza, C., & Zeippen, C. J. 1982, *MNRAS*, 198, 127, doi: [10.1093/mnras/198.1.127](https://doi.org/10.1093/mnras/198.1.127)
- . 1983, *MNRAS*, 202, 981, doi: [10.1093/mnras/202.4.981](https://doi.org/10.1093/mnras/202.4.981)
- Mesa-Delgado, A., Esteban, C., & García-Rojas, J. 2008, *ApJ*, 675, 389, doi: [10.1086/524296](https://doi.org/10.1086/524296)
- Mesa-Delgado, A., Esteban, C., García-Rojas, J., et al. 2009, *MNRAS*, 395, 855, doi: [10.1111/j.1365-2966.2009.14554.x](https://doi.org/10.1111/j.1365-2966.2009.14554.x)
- Moehler, S., Dreizler, S., LeBlanc, F., et al. 2014a, *A&A*, 565, A100, doi: [10.1051/0004-6361/201322953](https://doi.org/10.1051/0004-6361/201322953)
- Moehler, S., Modigliani, A., Freudling, W., et al. 2014b, *A&A*, 568, A9, doi: [10.1051/0004-6361/201423790](https://doi.org/10.1051/0004-6361/201423790)
- Morisset, C. 2017, in Planetary Nebulae: Multi-Wavelength Probes of Stellar and Galactic Evolution, ed. X. Liu, L. Stanghellini, & A. Karakas, Vol. 323, 43–50, doi: [10.1017/S1743921317001004](https://doi.org/10.1017/S1743921317001004)
- Muench, A. A., Lada, E. A., Lada, C. J., & Alves, J. 2002, *ApJ*, 573, 366, doi: [10.1086/340554](https://doi.org/10.1086/340554)
- Münch, G., & Wilson, O. C. 1962, *ZA*, 56, 127
- Nahar, S. N., & Pradhan, A. K. 1996, *A&AS*, 119, 509
- Núñez-Díaz, M., Mesa-Delgado, A., Esteban, C., et al. 2012, *MNRAS*, 421, 3399, doi: [10.1111/j.1365-2966.2012.20565.x](https://doi.org/10.1111/j.1365-2966.2012.20565.x)
- Nussbaumer, H., & Storey, P. J. 1982, *A&A*, 110, 295
- O'Dell, C. R. 2009, *PASP*, 121, 428, doi: [10.1086/599242](https://doi.org/10.1086/599242)
- . 2018, *MNRAS*, 478, 1017, doi: [10.1093/mnras/sty960](https://doi.org/10.1093/mnras/sty960)
- O'Dell, C. R., Abel, N. P., & Ferland, G. J. 2020, *ApJ*, 891, 46, doi: [10.3847/1538-4357/ab723d](https://doi.org/10.3847/1538-4357/ab723d)
- O'Dell, C. R., & Doi, T. 2003, *AJ*, 125, 277, doi: [10.1086/345512](https://doi.org/10.1086/345512)
- O'Dell, C. R., Ferland, G. J., & Henney, W. J. 2001, *ApJ*, 556, 203, doi: [10.1086/321562](https://doi.org/10.1086/321562)
- O'Dell, C. R., Ferland, G. J., Henney, W. J., et al. 2015, *AJ*, 150, 108, doi: [10.1088/0004-6256/150/4/108](https://doi.org/10.1088/0004-6256/150/4/108)
- O'Dell, C. R., Ferland, G. J., & Peimbert, M. 2017a, *MNRAS*, 464, 4835, doi: [10.1093/mnras/stw2713](https://doi.org/10.1093/mnras/stw2713)
- O'Dell, C. R., Hartigan, P., Bally, J., & Morse, J. A. 1997a, *AJ*, 114, 2016, doi: [10.1086/118622](https://doi.org/10.1086/118622)
- O'Dell, C. R., Hartigan, P., Lane, W. M., et al. 1997b, *AJ*, 114, 730, doi: [10.1086/118507](https://doi.org/10.1086/118507)
- O'Dell, C. R., Kollatschny, W., & Ferland, G. J. 2017b, *ApJ*, 837, 151, doi: [10.3847/1538-4357/aa6198](https://doi.org/10.3847/1538-4357/aa6198)
- O'Dell, C. R., Peimbert, M., & Peimbert, A. 2003, *AJ*, 125, 2590, doi: [10.1086/374788](https://doi.org/10.1086/374788)
- O'Dell, C. R., & Wong, K. 1996, *AJ*, 111, 846, doi: [10.1086/117832](https://doi.org/10.1086/117832)
- Osterbrock, D. E., Tran, H. D., & Veilleux, S. 1992, *ApJ*, 389, 305, doi: [10.1086/171206](https://doi.org/10.1086/171206)
- Peimbert, M. 1967, *ApJ*, 150, 825, doi: [10.1086/149385](https://doi.org/10.1086/149385)
- Pequignot, D., Petitjean, P., & Boisson, C. 1991, *A&A*, 251, 680
- Podobedova, L. I., Kelleher, D. E., & Wiese, W. L. 2009, Journal of Physical and Chemical Reference Data, 38, 171
- Porter, R. L., Ferland, G. J., Storey, P. J., & Detisch, M. J. 2012, *MNRAS*, 425, L28, doi: [10.1111/j.1745-3933.2012.01300.x](https://doi.org/10.1111/j.1745-3933.2012.01300.x)
- . 2013, *MNRAS*, 433, L89, doi: [10.1093/mnrasl/slt049](https://doi.org/10.1093/mnrasl/slt049)
- Quinet, P. 1996, *A&AS*, 116, 573
- Quinet, P., & Le Dourneuf, M. 1996, *A&AS*, 119, 99
- Ramsbottom, C. A., & Bell, K. L. 1997, *Atomic Data and Nuclear Data Tables*, 66, 65, doi: [10.1006/adnd.1997.0741](https://doi.org/10.1006/adnd.1997.0741)
- Rodríguez, M. 1999, *A&A*, 348, 222, <https://arxiv.org/abs/astro-ph/9906291>
- Rodríguez, M., & Rubin, R. H. 2005, *ApJ*, 626, 900, doi: [10.1086/429958](https://doi.org/10.1086/429958)
- Rosado, M., de La Fuente, E., Arias, L., & Le Coarer, E. 2002, in Revista Mexicana de Astronomía y Astrofísica Conference Series, Vol. 13, Revista Mexicana de Astronomía y Astrofísica Conference Series, ed. W. J. Henney, W. Steffen, L. Binette, & A. Raga, 90–93, <https://arxiv.org/abs/astro-ph/0107439>
- Simón-Díaz, S. 2010, *A&A*, 510, A22, doi: [10.1051/0004-6361/200913120](https://doi.org/10.1051/0004-6361/200913120)
- Simón-Díaz, S., García-Rojas, J., Esteban, C., et al. 2011, *A&A*, 530, A57, doi: [10.1051/0004-6361/201116608](https://doi.org/10.1051/0004-6361/201116608)
- Stasińska, G. 1978, *A&A*, 66, 257
- Storey, P. J., & Hummer, D. G. 1995, *MNRAS*, 272, 41, doi: [10.1093/mnras/272.1.41](https://doi.org/10.1093/mnras/272.1.41)
- Storey, P. J., Sochi, T., & Badnell, N. R. 2014, *MNRAS*, 441, 3028, doi: [10.1093/mnras/stu777](https://doi.org/10.1093/mnras/stu777)
- Storey, P. J., Sochi, T., & Bastin, R. 2017, *MNRAS*, 470, 379, doi: [10.1093/mnras/stx1189](https://doi.org/10.1093/mnras/stx1189)
- Storey, P. J., & Zeippen, C. J. 2000, *MNRAS*, 312, 813, doi: [10.1046/j.1365-8711.2000.03184.x](https://doi.org/10.1046/j.1365-8711.2000.03184.x)
- Sutherland, R. S., & Dopita, M. A. 2017, *ApJS*, 229, 34, doi: [10.3847/1538-4365/aa6541](https://doi.org/10.3847/1538-4365/aa6541)
- Takami, M., Usuda, T., Sugai, H., et al. 2002, *ApJ*, 566, 910, doi: [10.1086/338245](https://doi.org/10.1086/338245)
- Tayal, S. S. 2004, *A&A*, 418, 363, doi: [10.1051/0004-6361:20034384](https://doi.org/10.1051/0004-6361:20034384)
- . 2011, *ApJS*, 195, 12, doi: [10.1088/0067-0049/195/2/12](https://doi.org/10.1088/0067-0049/195/2/12)
- Tayal, S. S., & Zatsarinny, O. 2010, *ApJS*, 188, 32, doi: [10.1088/0067-0049/188/1/32](https://doi.org/10.1088/0067-0049/188/1/32)
- . 2020, *ApJ*, 888, 10, doi: [10.3847/1538-4357/ab557b](https://doi.org/10.3847/1538-4357/ab557b)

- Tody, D. 1993, Astronomical Society of the Pacific Conference Series, Vol. 52, IRAF in the Nineties, ed. R. J. Hanisch, R. J. V. Brissenden, & J. Barnes, 173
- Torres-Peimbert, S., Peimbert, M., & Daltabuit, E. 1980, ApJ, 238, 133, doi: [10.1086/157966](https://doi.org/10.1086/157966)
- van der Werf, P. P., Goss, W. M., & O'Dell, C. R. 2013, ApJ, 762, 101, doi: [10.1088/0004-637X/762/2/101](https://doi.org/10.1088/0004-637X/762/2/101)
- Verner, E. M., Verner, D. A., Baldwin, J. A., Ferland , G. J., & Martin, P. G. 2000, ApJ, 543, 831, doi: [10.1086/317159](https://doi.org/10.1086/317159)
- Weilbacher, P. M., Monreal-Ibero, A., Kollatschny, W., et al. 2015, A&A, 582, A114, doi: [10.1051/0004-6361/201526529](https://doi.org/10.1051/0004-6361/201526529)
- Wiese, W. L., Fuhr, J. R., & Deters, T. M. 1996, Journal of Physical and Chemical Reference Data, Monograph 7, 403
- Zel'dovich, Y. B., & Raizer, Y. P. 1967, Physics of shock waves and high-temperature hydrodynamic phenomena
- Zhang, H. L., & Pradhan, A. K. 1997, A&AS, 126, 373
- Zhang, Hong Lin. 1996, Astron. Astrophys. Suppl. Ser., 119, 523, doi: [10.1051/aas:1996264](https://doi.org/10.1051/aas:1996264)

APPENDIX

A. HOW RELIABLE ARE THE ATOMIC DATA OF [FE III] THAT WE USE?

Generally, the discrepancy between the physical conditions derived from diagnostics based on [Fe III] lines and those estimated from other ions has been interpreted as a result of errors in the transition probabilities and/or in the collision strengths of the Fe^{2+} ion (See the introduction of Laha et al. 2017). With HH 204 we have an excellent opportunity to test the reliability of the atomic data we use for this ion for the following reasons: (i) we have enough spectral resolution to separate the emission of HH 204 from that of the Orion Nebula. (ii) Owing to its geometry and 3D trajectory, we do not expect significant inhomogeneities in the physical conditions within the line of sight. Due to this, all the density diagnostics used in Table 3 are consistent with each other, while the global gas temperature, due to the low degree of ionization, is well represented by $T_e(\text{[N II]})$. (iii) The [Fe III] emission is enhanced owing to the destruction of dust grains containing Fe atoms in the shock, which allows to have a good signal to noise even for some weak lines that are difficult to detect.

We have used a set of transition probabilities compiled in PyNeb, which includes the data from Quinet (1996) and those from Johansson et al. (2000) for ${}^5\text{D} - {}^5\text{S}_2$ transitions. However, these transitions produce lines out of the spectral range covered by our observation, so we finally only use the calculations from Quinet (1996). Table 12 shows that the transition probabilities we use are in good agreement with the observed intensity ratios of lines arising from the same upper level in the case of lines used to determine physical conditions. However, the intensity ratios between lines that arise from different upper levels do depend on n_e and T_e . As discussed above and in Sec. 9.4, in HH 204 there are no significant density inhomogeneities that may produce a bias in some diagnostics, contrary to the case analyzed in Sec. 7. Thus, all the density diagnostics included in Table 3 give consistent results, and the average of $n_e(\text{[O II]})$, $n_e(\text{[S II]})$, $n_e(\text{[Cl III]})$ and $n_e(\text{[Fe II]})$ is $n_e = 13330 \pm 550$. Using this density for its calculation, $T_e(\text{[N II]})$ remains practically unchanged from what is shown in Table 3. Considering these values of n_e and $T_e(\text{[N II]})$, we can check the validity of [Fe III] atomic data by applying the procedure that we describe below. Firstly, we take into account all the observed [Fe III] lines that are not affected by blending with other lines, sky features or telluric absorptions. Then we normalize their emission with respect to $I(\text{[Fe III]} \lambda 4658)/I(\text{H}\beta) = 1000$. Moreover, we also discard the [Fe III] $\lambda\lambda 3355.50, 7078.22$ lines, since their FWHM are much wider than the rest of [Fe III] lines, which is indicative of line blending. [Fe III] $\lambda 9203.85$ is also discarded because it shows a radial velocity of $\sim 10 \text{ km s}^{-1}$, larger than the velocities of the rest of [Fe III] lines, which may be indicative of a doubtful identification. We also discard [Fe III] $\lambda 8838.14$ because, although we deblend it from a very close sky feature, its intensity may not be completely reliable. Once we have the set of [Fe III] lines with confident observed intensity ratios, they were compared with the predictions of the atomic data for the assumed physical conditions and considering error propagation. The results are shown in Table 14.

Table 14 does not include 5D – 7S transitions ([Fe III] $\lambda\lambda 3322.47, 3371.35, 3406.18$ lines) because their transition probabilities are not calculated in the reference of the atomic data used (their “Predicted” and “Difference” columns are empty). However, their measured intensities can be used to check other atomic data sets that do include them. In general, Table 14 shows good agreement between predicted and observed intensity ratios of [Fe III] lines. Only 4 lines ($\lambda\lambda 4008.34, 4079.69, 4985.88, 7088.46$) show differences larger than 10%, exceeding the error bars. This can be attributed to errors in their atomic data. The first two lines arise from the same ${}^3\text{G}_4$ upper level, so their intensity ratio only depends on their transition probabilities. Although the $I(\text{[Fe III]} \lambda 4008.34)/I(\text{[Fe III]} \lambda 4079.69)$ ratio is not included in Table 12 – these lines were not used to determine physical conditions – its intensity ratio of 4.43 ± 0.30 is larger than the theoretical one of 3.92. Therefore it is plausible that part of the observed discrepancy is due to incorrect transition probabilities. The largest differences reported in Table 14 are for [Fe III] $\lambda\lambda 4985.88, 7088.46$ lines, but we can not find an obvious explanation for this. In addition to the atomic data used, we have checked other sets. For transition probabilities: Nahar & Pradhan (1996); Bautista et al. (2010). For collision strengths: Bautista et al. (2010); Badnell & Ballance (2014). We have tried all possible combinations of these data. Of the 9 combinations, the atomic data we use in this paper minimizes the difference between the predicted and measured intensity ratios. The results of this appendix indicate that the atomic data used in this work for [Fe III] lines contribute little to errors in the derived physical conditions and the Fe^{2+} abundances, at least for the conditions of HH 204. As we discuss in Sec. 7 the discrepancy normally found between $n_e(\text{[Fe III]})$ and the classical diagnostics – as $n_e(\text{[O II]})$ or $n_e(\text{[S II]})$ –

Table 9: Sample of 15 lines from the spectra of cut 1.

λ_0 (Å)	Ion	λ_{obs}	HH 204				The Orion Nebula+The Diffuse Blue Layer							
			Vel(λ_0) (Km s $^{-1}$)	FWHM (Km s $^{-1}$)	F(λ)/F(H β)	I(λ)/I(H β)	Err %	λ_{obs}	Vel(λ_0) (Km s $^{-1}$)	FWHM (Km s $^{-1}$)	F(λ)/F(H β)	I(λ)/I(H β)	Err %	Notes
4701.64	[Fe III]	4701.25	-24.76	18.30 ± 0.02	1.424	1.460	2	4701.83	12.22	23.27 ± 0.33	0.193	0.197	3	
4713.14	He I	4712.80	-21.48	18.57 ± 0.31	0.206	0.211	3	4713.35	13.51	27.03 ± 0.30	0.436	0.443	3	
4728.07	[Fe II]	4727.75	-20.08	13.57 ± 0.36	0.072	0.073	4	4728.45	24.31	8.18 ± 4.17	0.004	0.004	30	
4734.00	[Fe III]	4733.57	-27.00	18.18 ± 0.05	0.634	0.647	2	4734.15	9.74	23.81 ± 1.68	0.067	0.068	6	
4740.17	[Ar IV]	*	*	*	*	*	*	4740.35	11.65	14.86 ± 6.68	0.006	0.006	29	
4754.81	[Fe III]	4754.42	-24.90	18.29 ± 0.04	0.800	0.813	2	4755.00	11.67	22.95 ± 0.58	0.127	0.128	4	
4769.53	[Fe III]	4769.14	-24.77	18.23 ± 0.04	0.505	0.512	2	4769.73	12.32	22.75 ± 0.72	0.064	0.065	4	
4774.73	[Fe II]	4774.42	-19.69	13.19 ± 0.51	0.070	0.071	4	*	*	*	*	*	*	
4777.70	[Fe III]	4777.38	-20.30	17.82 ± 0.21	0.304	0.308	3	4777.97	16.73	24.34 ± 2.76	0.032	0.032	10	
4803.29	N II	*	*	*	*	*	*	4803.46	10.50	18.10 ± 2.08	0.019	0.019	8	
4814.54	[Fe II]	4814.23	-19.37	14.38 ± 0.04	0.393	0.396	2	*	*	*	*	*	*	
4874.50	[Fe II]	4874.18	-19.51	13.84 ± 0.54	0.051	0.051	4	*	*	*	*	*	*	
4861.32	H I	4860.97	-21.47	24.67 ± 0.01	100.000	100.000	2	4861.52	12.45	30.59 ± 0.01	100.000	100.000	2	
4861.32	H I	4859.66	-102.26	14.31 ± 1.90	0.106	0.106	10	*	*	*	*	*	*	Deuterium
4874.50	[Fe II]	4874.18	-19.51	13.84 ± 0.54	0.051	0.051	4	*	*	*	*	*	*	
4881.07	[Fe III]	4880.71	-21.92	18.00 ± 0.01	2.251	2.245	2	4881.30	14.32	20.70 ± 0.17	0.248	0.247	3	

may be rather an indicative of the presence of high-density inclusions within the line of sight. For a complete test of the atomic data, similar studies would be necessary in different ranges of physical conditions. We will continue to investigate this in other HH objects in future papers of this series.

B. SUPPORTING MATERIAL

In this appendix we include the following material:

- Fig. 24: Plasma diagnostics for the individual components analyzed in this work.
- Table 9: Sample of lines of the spectra of cut 1 as found in the online material.
- Table 10: Atomic data set used for CELs.
- Table 11: Atomic data set used for RLs.
- Table 12: Measured and predicted [Fe III] intensity ratios from lines that arise from a common upper level.
- Table 13: Measured and predicted [Fe II] intensity ratios from lines that arise from a common upper level.
- Table 14: Measured and predicted [Fe III] intensity ratios for all detected lines, using the atomic data chosen in this work.
- Table 15: Pixel-to-pixel spatial distribution of the physical conditions and ionic abundances of HH 204 in the UVES blue arm spectra.
- Table 16: Pixel-to-pixel spatial distribution of the physical conditions and ionic abundances of HH 204 in the UVES red arm spectra.
- Table 17: Pixel-to-pixel spatial distribution of ionic abundances of HH 204 in the UVES red arm spectra.

Table 10: Atomic data set used for collisionally excited lines.

Ion	Transition Probabilities	Collision Strengths
O ⁰	Wiese et al. (1996)	Bhatia & Kastner (1995)
O ⁺	Froese Fischer & Tachiev (2004)	Kisielius et al. (2009)
O ²⁺	Wiese et al. (1996), Storey & Zeippen (2000)	Storey et al. (2014)
N ⁺	Froese Fischer & Tachiev (2004)	Tayal (2011)
Ne ²⁺	McLaughlin et al. (2011)	McLaughlin et al. (2011)
S ⁺	Podobedova et al. (2009)	Tayal & Zatsarinny (2010)
S ²⁺	Podobedova et al. (2009)	Grieve et al. (2014)
Cl ⁺	Mendoza & Zeippen (1983)	Tayal (2004)
Cl ²⁺	Fritzsche et al. (1999)	Butler & Zeippen (1989)
Ar ²⁺	Mendoza (1983), Kaufman & Sugar (1986)	Galavis, Mendoza, & Zeippen (1995)
Ar ³⁺	Mendoza & Zeippen (1982)	Ramsbottom & Bell (1997)
Fe ⁺	Bautista et al. (2015)	Bautista et al. (2015)
Fe ²⁺	Quinet (1996) , Johansson et al. (2000)	Zhang, Hong Lin (1996)
Fe ³⁺	Froese Fischer et al. (2008)	Zhang & Pradhan (1997)
Ni ⁺	Quinet & Le Dourneuf (1996), Nussbaumer & Storey (1982)	Bautista (2004)
Ni ²⁺	Bautista (2001)	Bautista (2001)
Ca ⁺	Meléndez et al. (2007)	Meléndez et al. (2007)
Cr ⁺	Tayal & Zatsarinny (2020)	Tayal & Zatsarinny (2020)

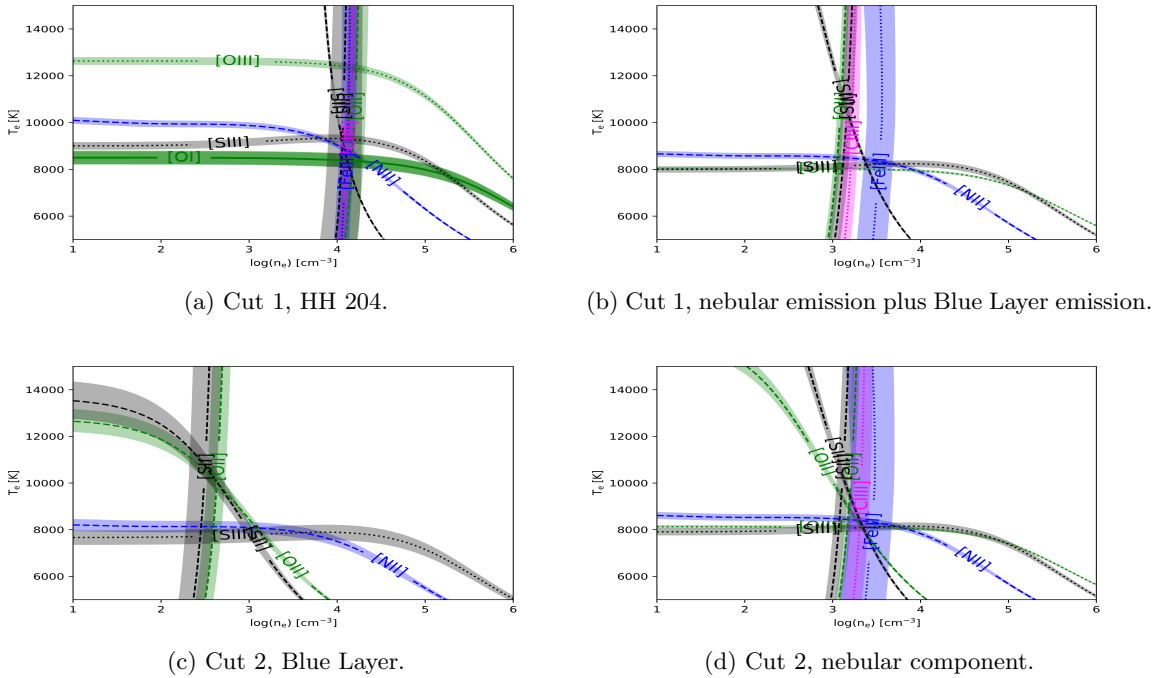
**Figure 24:** Plasma diagnostic plots for the individual analyzed components. The labeled diagnostics correspond to those discussed in Sec. 4.1.

Table 11: Effective recombination coefficients used for recombination lines.

Ion	Reference
H ⁺	Storey & Hummer (1995)
He ⁺	Porter et al. (2012, 2013)
O ⁺	Pequignot et al. (1991)
O ²⁺	Storey et al. (2017)
C ²⁺	Davey et al. (2000)

Table 13: Comparison of the observed [Fe II] intensity ratios in HH 204 and theoretical ones predicted by the transition probabilities of Bautista et al. (2015).

Line ratio	HH 204	Prediction
9052/9399	5.45 ± 0.48	5.49
9052/7927	18.84 ± 1.99	6.91
8892/9227	1.71 ± 0.11	1.80
8892/7874	28.58 ± 4.15	10.64
8892/7687	3.85 ± 0.22	1.48
9268/9034*	1.33 ± 0.09	1.28
9268/7733*	11.72 ± 1.37	5.08

NOTE—* [Fe II] λ 9267.56 was deblended from a sky emission.

Table 12: Comparison of the observed [Fe III] intensity ratios in HH 204 and theoretical ones predicted by the transition probabilities of Quinet (1996) and Johansson et al. (2000).

Line ratio	HH 204	Prediction
3240/3286	3.63 ± 0.81	3.60
3240/3319	3.63 ± 0.86	5.06
3240/8729*	11.35 ± 1.06	11.87
3335/3357	1.16 ± 0.20	1.18
3335/8838**	6.15 ± 1.00	4.93
4607/4702	0.18 ± 0.01	0.17
4607/4770	0.51 ± 0.01	0.51
4667/4734	0.29 ± 0.01	0.28
4667/4778	0.60 ± 0.03	0.57
4658/4755	5.33 ± 0.15	5.49
4881/4987	6.07 ± 0.17	5.76
5011/5085	5.85 ± 0.32	5.94
5271/5412	10.75 ± 0.39	11.01

NOTE—* The emission of [Fe III] λ 8728.84 from HH 204 was deblended from the nebular component of [C I] λ 8727.13.

** The emission of [Fe III] λ 8838.14 was deblended from a sky feature.

Table 14: Comparison between predicted and measured [Fe III] intensity ratios with the chosen atomic data. The intensities are normalized to $I([\text{Fe III}])\lambda 4658 = 1000$.

λ (Å)	Predicted $I(\lambda)/I(4658)$	Measured $I(\lambda)/I(4658)$	Difference
3239.79	90.3 ± 3.1	84.6 ± 6.3	-7% \pm 8%
3286.24	25.1 ± 0.9	22.3 ± 4.9	-13% \pm 30%
3319.27	17.8 ± 0.6	22.9 ± 4.5	23% \pm 16%
3322.47	-	103.0 ± 7.0	-
3334.95	32.1 ± 1.1	28.8 ± 3.8	-14% \pm 17%
3356.59	27.2 ± 0.9	24.5 ± 2.0	-9% \pm 9%
3366.22	14.6 ± 0.5	18.5 ± 2.5	21% \pm 12%
3371.35	-	67.9 ± 4.4	-
3406.18	-	39.1 ± 3.3	-
4008.34	57.4 ± 0.7	50.0 ± 1.6	-14% \pm 3%
4046.49	8.2 ± 0.1	7.7 ± 0.7	-6% \pm 10%
4079.69	14.6 ± 0.2	11.2 ± 0.8	-30% \pm 7%
4096.68	3.2 ± 0.1	2.3 ± 0.4	-37% \pm 30%
4607.12	58.5 ± 0.3	60.3 ± 1.5	2% \pm 2%
4667.11	40.4 ± 0.5	43.1 ± 1.6	6% \pm 3%
4701.64	338.5 ± 1.9	336.9 ± 10.3	0% \pm 3%
4734.00	146.1 ± 1.6	150.8 ± 3.4	3% \pm 2%
4754.81	182.1 ± 0.0	187.3 ± 5.7	3% \pm 3%
4769.53	115.3 ± 0.7	118.2 ± 3.2	2% \pm 2%
4777.70	70.3 ± 0.8	71.4 ± 2.4	0% \pm 3%
4881.07	484.3 ± 2.1	519.0 ± 15.3	7% \pm 2%
4924.66	6.6 ± 0.2	6.8 ± 0.5	1% \pm 7%
4930.64	40.3 ± 0.6	43.6 ± 1.7	7% \pm 3%
4985.88	15.5 ± 0.7	8.1 ± 0.6	-91% \pm 15%
4987.29	84.1 ± 0.4	85.2 ± 2.3	1% \pm 2%
5011.41	143.1 ± 1.3	147.4 ± 4.5	1% \pm 2%
5084.85	24.1 ± 0.2	25.0 ± 1.3	4% \pm 5%
5270.57	487.8 ± 3.8	525.0 ± 14.5	6% \pm 2%
5412.06	44.3 ± 0.3	48.9 ± 1.9	9% \pm 3%
7088.46	1.1 ± 0.1	1.8 ± 0.2	39% \pm 6%
8728.84	7.6 ± 0.3	7.3 ± 0.4	-3% \pm 7%
9701.87	24.6 ± 0.7	24.8 ± 1.1	0% \pm 5%
9942.38	15.9 ± 0.5	18.3 ± 1.4	13% \pm 6%

Table 15: Spatial distribution of physical conditions and ionic abundances along HH 204 as a function of the distance from the bowshock. Values derived from the blue arm spectrum.

Distance (mpc)	n_e ([Fe III]) (cm $^{-3}$)	T_e ([O III]) (K)	He $^+$ ($\lambda 4471$)	O $^+$	O $^{2+}$	Ne $^{2+}$
0.00	21180 \pm 5900	16790 \pm 700	10.50 \pm 0.02	8.72 \pm 0.14	6.13 \pm 0.05	-
0.49	19020 \pm 5160	17200 \pm 600	10.46 \pm 0.01	8.64 \pm 0.12	6.02 \pm 0.04	-
0.98	19610 \pm 4530	18510 \pm 560	10.46 \pm 0.01	8.72 \pm 0.10	5.89 \pm 0.03	-
1.47	21810 \pm 3940	15620 \pm 470	10.46 \pm 0.01	8.67 \pm 0.10	6.05 \pm 0.04	-
1.96	15930 \pm 4160	15200 \pm 580	10.43 \pm 0.01	8.61 \pm 0.09	6.07 \pm 0.04	-
2.44	16170 \pm 3370	15880 \pm 580	10.41 \pm 0.01	8.62 \pm 0.07	5.94 \pm 0.04	-
2.93	14040 \pm 2220	14730 \pm 460	10.39 \pm 0.01	8.56 \pm 0.07	5.99 \pm 0.04	-
3.42	17480 \pm 3310	14660 \pm 420	10.38 \pm 0.01	8.65 \pm 0.08	5.99 \pm 0.03	-
3.91	15800 \pm 2990	13990 \pm 350	10.39 \pm 0.01	8.59 \pm 0.10	6.03 \pm 0.03	-
4.40	13600 \pm 2530	13480 \pm 460	10.41 \pm 0.01	8.56 \pm 0.08	6.06 \pm 0.04	-
4.89	14800 \pm 2630	12430 \pm 380	10.38 \pm 0.01	8.62 \pm 0.08	6.17 \pm 0.04	-
5.38	13680 \pm 2760	12020 \pm 390	10.38 \pm 0.01	8.57 \pm 0.08	6.22 \pm 0.05	-
5.87	12210 \pm 2730	11910 \pm 360	10.41 \pm 0.01	8.52 \pm 0.08	6.25 \pm 0.04	-
6.36	13180 \pm 2480	11300 \pm 340	10.41 \pm 0.01	8.56 \pm 0.06	6.32 \pm 0.04	-
6.85	12270 \pm 2580	11600 \pm 310	10.44 \pm 0.01	8.57 \pm 0.09	6.31 \pm 0.04	4.99 \pm 0.07
7.33	13740 \pm 2610	11500 \pm 390	10.45 \pm 0.01	8.61 \pm 0.08	6.34 \pm 0.05	5.12 \pm 0.07
7.82	13440 \pm 2520	11470 \pm 290	10.45 \pm 0.01	8.56 \pm 0.08	6.36 \pm 0.04	5.14 \pm 0.06
8.31	14040 \pm 2450	11630 \pm 340	10.45 \pm 0.01	8.58 \pm 0.07	6.33 \pm 0.04	5.14 \pm 0.07
8.80	11630 \pm 2200	11260 \pm 250	10.44 \pm 0.01	8.51 \pm 0.07	6.39 \pm 0.03	5.16 \pm 0.06
9.29	13490 \pm 2450	11450 \pm 260	10.47 \pm 0.01	8.51 \pm 0.08	6.41 \pm 0.04	5.19 \pm 0.05
9.78	11960 \pm 2490	11230 \pm 280	10.52 \pm 0.01	8.54 \pm 0.07	6.50 \pm 0.03	5.25 \pm 0.06
10.27	11400 \pm 2390	11620 \pm 220	10.58 \pm 0.01	8.52 \pm 0.07	6.51 \pm 0.03	5.23 \pm 0.05
10.76	11420 \pm 2190	12020 \pm 280	10.64 \pm 0.01	8.51 \pm 0.07	6.49 \pm 0.03	5.24 \pm 0.05
11.25	9490 \pm 1970	11530 \pm 310	10.70 \pm 0.01	8.48 \pm 0.06	6.62 \pm 0.04	5.41 \pm 0.06
11.74	10400 \pm 1980	11710 \pm 250	10.75 \pm 0.01	8.53 \pm 0.07	6.63 \pm 0.03	5.41 \pm 0.06
12.22	10330 \pm 2020	11550 \pm 200	10.80 \pm 0.01	8.53 \pm 0.07	6.71 \pm 0.02	5.54 \pm 0.04
12.71	9740 \pm 1970	11030 \pm 240	10.84 \pm 0.01	8.50 \pm 0.07	6.84 \pm 0.03	5.61 \pm 0.05

NOTE—Abundances in units of $12 + \log(X^{n+}/H^+)$

Table 16: Spatial distribution of physical conditions and ionic abundances along HH 204 as a function of the distance from the bowshock. Values derived from the red arm spectrum.

Distance (mpc)	T_e ([N II]) (K)	T_e ([S III]) (K)	He^+ ($\lambda 5876$)	He^+ ($\lambda 6678$)	N^+	O^+ (RLs)	S^+	S^{2+}
0.29	8780 ± 310	9150 ± 190	10.41 ± 0.01	10.57 ± 0.03	7.79 ± 0.06	8.68 ± 0.15	6.82 ± 0.09	6.84 ± 0.03
0.66	8970 ± 340	8780 ± 180	10.43 ± 0.01	10.51 ± 0.03	7.75 ± 0.05	8.87 ± 0.11	6.77 ± 0.08	6.90 ± 0.03
1.02	8670 ± 280	9140 ± 210	10.43 ± 0.01	10.50 ± 0.02	7.80 ± 0.05	-	6.82 ± 0.09	6.83 ± 0.03
1.38	8920 ± 300	9500 ± 220	10.42 ± 0.01	10.48 ± 0.02	7.75 ± 0.05	8.75 ± 0.12	6.78 ± 0.08	6.77 ± 0.03
1.74	9100 ± 290	9390 ± 190	10.42 ± 0.01	10.43 ± 0.02	7.71 ± 0.04	-	6.73 ± 0.07	6.78 ± 0.02
2.10	8860 ± 290	9050 ± 200	10.41 ± 0.01	10.48 ± 0.02	7.73 ± 0.05	8.57 ± 0.15	6.73 ± 0.08	6.82 ± 0.02
2.46	8980 ± 220	9290 ± 210	10.39 ± 0.01	10.45 ± 0.02	7.73 ± 0.04	8.80 ± 0.09	6.74 ± 0.06	6.82 ± 0.03
2.83	8850 ± 220	9420 ± 170	10.37 ± 0.01	10.43 ± 0.02	7.73 ± 0.03	8.70 ± 0.09	6.72 ± 0.07	6.78 ± 0.02
3.19	8750 ± 230	9250 ± 180	10.37 ± 0.01	10.39 ± 0.02	7.75 ± 0.04	8.72 ± 0.07	6.76 ± 0.07	6.77 ± 0.03
3.55	8790 ± 190	9410 ± 180	10.36 ± 0.01	10.43 ± 0.02	7.75 ± 0.04	8.68 ± 0.07	6.79 ± 0.07	6.75 ± 0.02
3.91	8860 ± 260	9410 ± 180	10.36 ± 0.01	10.42 ± 0.02	7.75 ± 0.04	8.66 ± 0.07	6.78 ± 0.07	6.74 ± 0.03
4.27	8900 ± 230	9390 ± 190	10.37 ± 0.01	10.42 ± 0.02	7.74 ± 0.04	8.74 ± 0.06	6.75 ± 0.06	6.74 ± 0.03
4.64	8800 ± 230	9430 ± 190	10.36 ± 0.01	10.41 ± 0.02	7.75 ± 0.04	8.79 ± 0.06	6.72 ± 0.06	6.73 ± 0.02
5.00	8760 ± 230	9400 ± 190	10.34 ± 0.01	10.40 ± 0.02	7.74 ± 0.04	8.74 ± 0.07	6.72 ± 0.06	6.72 ± 0.03
5.36	8960 ± 220	9480 ± 190	10.36 ± 0.01	10.41 ± 0.02	7.71 ± 0.04	8.72 ± 0.06	6.66 ± 0.06	6.71 ± 0.02
5.72	8880 ± 210	9310 ± 190	10.36 ± 0.01	10.42 ± 0.02	7.72 ± 0.04	8.71 ± 0.06	6.63 ± 0.08	6.74 ± 0.03
6.08	8800 ± 220	9330 ± 180	10.36 ± 0.01	10.42 ± 0.02	7.74 ± 0.04	8.73 ± 0.05	6.67 ± 0.06	6.74 ± 0.03
6.44	8810 ± 220	9280 ± 180	10.38 ± 0.01	10.42 ± 0.02	7.73 ± 0.04	8.64 ± 0.06	6.66 ± 0.07	6.76 ± 0.02
6.81	8760 ± 210	9240 ± 210	10.39 ± 0.01	10.43 ± 0.02	7.72 ± 0.04	8.65 ± 0.06	6.61 ± 0.07	6.76 ± 0.03
7.17	8790 ± 240	9290 ± 200	10.40 ± 0.01	10.44 ± 0.02	7.70 ± 0.04	8.73 ± 0.04	6.61 ± 0.06	6.75 ± 0.03
7.53	8840 ± 220	9480 ± 170	10.42 ± 0.01	10.45 ± 0.02	7.70 ± 0.03	8.56 ± 0.06	6.57 ± 0.06	6.71 ± 0.02
7.89	8830 ± 250	9500 ± 180	10.40 ± 0.01	10.45 ± 0.01	7.68 ± 0.04	8.57 ± 0.06	6.56 ± 0.07	6.71 ± 0.02
8.25	8800 ± 270	9410 ± 190	10.41 ± 0.01	10.46 ± 0.02	7.71 ± 0.04	8.62 ± 0.06	6.58 ± 0.07	6.73 ± 0.02
8.61	8830 ± 220	9360 ± 200	10.41 ± 0.01	10.46 ± 0.02	7.70 ± 0.04	8.64 ± 0.05	6.56 ± 0.07	6.75 ± 0.02
8.98	8870 ± 230	9370 ± 160	10.42 ± 0.02	10.47 ± 0.02	7.70 ± 0.03	8.56 ± 0.10	6.53 ± 0.06	6.77 ± 0.02
9.34	8920 ± 210	9220 ± 180	10.44 ± 0.01	10.48 ± 0.02	7.70 ± 0.03	8.61 ± 0.06	6.53 ± 0.06	6.80 ± 0.02
9.70	8860 ± 210	9410 ± 200	10.45 ± 0.01	10.49 ± 0.01	7.70 ± 0.04	8.63 ± 0.05	6.52 ± 0.06	6.77 ± 0.03
10.06	8800 ± 210	9570 ± 160	10.47 ± 0.01	10.51 ± 0.01	7.69 ± 0.03	8.60 ± 0.05	6.47 ± 0.05	6.74 ± 0.02
10.42	8730 ± 210	9740 ± 210	10.49 ± 0.01	10.53 ± 0.01	7.69 ± 0.04	8.62 ± 0.06	6.41 ± 0.07	6.70 ± 0.03
10.79	8850 ± 210	9900 ± 200	10.54 ± 0.01	10.59 ± 0.01	7.65 ± 0.04	8.56 ± 0.07	6.34 ± 0.07	6.68 ± 0.03
11.15	8770 ± 210	9890 ± 220	10.59 ± 0.01	10.62 ± 0.02	7.65 ± 0.04	8.56 ± 0.08	6.27 ± 0.07	6.67 ± 0.03
11.51	8820 ± 210	9680 ± 210	10.63 ± 0.01	10.65 ± 0.01	7.64 ± 0.04	8.77 ± 0.11	6.23 ± 0.06	6.72 ± 0.02
11.87	8720 ± 220	9690 ± 190	10.68 ± 0.01	10.71 ± 0.01	7.64 ± 0.04	8.60 ± 0.07	6.24 ± 0.06	6.73 ± 0.03
12.23	8740 ± 200	9840 ± 200	10.73 ± 0.01	10.75 ± 0.02	7.64 ± 0.04	8.75 ± 0.06	6.24 ± 0.08	6.72 ± 0.02
12.59	8860 ± 190	9750 ± 210	10.76 ± 0.01	10.79 ± 0.01	7.60 ± 0.03	8.68 ± 0.09	6.18 ± 0.06	6.73 ± 0.03
12.96	8980 ± 200	9720 ± 190	10.80 ± 0.01	10.82 ± 0.01	7.57 ± 0.03	8.41 ± 0.13	6.12 ± 0.07	6.74 ± 0.02
13.32	8320 ± 270	9880 ± 200	10.82 ± 0.01	10.85 ± 0.01	7.53 ± 0.03	8.67 ± 0.09	6.07 ± 0.05	6.70 ± 0.02

NOTE—Abundances in units of $12 + \log(\text{X}^{n+}/\text{H}^+)$

Table 17: Further ionic abundances along HH 204 as a function of the distance from the bowshock. Values derived from the red arm spectrum.

Distance (mpc)	Cl ⁺	Cl ²⁺	Ar ²⁺	Ca ⁺	Cr ⁺	Fe ⁺	Fe ²⁺	Ni ⁺	Ni ²⁺
0.29	4.93 ± 0.05	4.63 ± 0.08	5.66 ± 0.05	3.64 ± 0.05	4.57 ± 0.06	6.35 ± 0.04	6.46 ± 0.06	5.08 ± 0.03	5.05 ± 0.07
0.66	4.92 ± 0.04	4.83 ± 0.08	5.66 ± 0.04	3.66 ± 0.05	4.59 ± 0.06	6.35 ± 0.04	6.42 ± 0.06	5.09 ± 0.03	5.07 ± 0.06
1.02	4.94 ± 0.03	4.74 ± 0.05	5.70 ± 0.04	3.64 ± 0.05	4.71 ± 0.05	6.32 ± 0.05	6.49 ± 0.05	5.08 ± 0.03	5.10 ± 0.05
1.38	4.84 ± 0.04	4.67 ± 0.06	5.64 ± 0.04	3.47 ± 0.06	4.59 ± 0.05	6.27 ± 0.05	6.45 ± 0.06	5.00 ± 0.03	5.06 ± 0.06
1.74	4.80 ± 0.04	4.72 ± 0.04	5.59 ± 0.03	3.54 ± 0.05	4.49 ± 0.04	6.17 ± 0.04	6.40 ± 0.05	4.97 ± 0.03	5.00 ± 0.06
2.10	4.82 ± 0.04	4.86 ± 0.05	5.61 ± 0.04	3.46 ± 0.04	4.53 ± 0.04	6.23 ± 0.05	6.43 ± 0.05	5.00 ± 0.03	5.04 ± 0.05
2.46	4.84 ± 0.04	4.84 ± 0.04	5.60 ± 0.03	3.53 ± 0.05	4.55 ± 0.04	6.26 ± 0.04	6.42 ± 0.04	5.03 ± 0.03	5.07 ± 0.05
2.83	4.82 ± 0.03	4.83 ± 0.04	5.59 ± 0.03	3.51 ± 0.04	4.58 ± 0.03	6.28 ± 0.03	6.46 ± 0.04	5.02 ± 0.03	5.03 ± 0.04
3.19	4.83 ± 0.03	4.80 ± 0.05	5.58 ± 0.03	3.52 ± 0.04	4.59 ± 0.04	6.28 ± 0.03	6.49 ± 0.05	5.07 ± 0.03	5.08 ± 0.05
3.55	4.83 ± 0.03	4.71 ± 0.05	5.56 ± 0.03	3.57 ± 0.04	4.58 ± 0.04	6.28 ± 0.03	6.46 ± 0.04	5.07 ± 0.02	5.05 ± 0.04
3.91	4.83 ± 0.03	4.73 ± 0.04	5.54 ± 0.04	3.56 ± 0.04	4.53 ± 0.04	6.29 ± 0.03	6.47 ± 0.05	5.06 ± 0.03	5.06 ± 0.05
4.27	4.81 ± 0.03	4.69 ± 0.05	5.55 ± 0.03	3.54 ± 0.04	4.49 ± 0.04	6.30 ± 0.03	6.46 ± 0.05	5.05 ± 0.03	5.09 ± 0.05
4.64	4.81 ± 0.03	4.73 ± 0.04	5.56 ± 0.03	3.54 ± 0.03	4.44 ± 0.03	6.32 ± 0.03	6.49 ± 0.04	5.03 ± 0.02	5.11 ± 0.04
5.00	4.80 ± 0.03	4.71 ± 0.04	5.56 ± 0.03	3.55 ± 0.04	4.46 ± 0.04	6.32 ± 0.04	6.50 ± 0.04	5.02 ± 0.03	5.11 ± 0.05
5.36	4.76 ± 0.04	4.68 ± 0.04	5.53 ± 0.03	3.50 ± 0.04	4.41 ± 0.03	6.27 ± 0.03	6.46 ± 0.04	4.99 ± 0.03	5.07 ± 0.04
5.72	4.77 ± 0.03	4.75 ± 0.04	5.55 ± 0.03	3.54 ± 0.04	4.36 ± 0.04	6.27 ± 0.03	6.49 ± 0.04	5.00 ± 0.02	5.12 ± 0.04
6.08	4.76 ± 0.03	4.71 ± 0.05	5.57 ± 0.03	3.55 ± 0.03	4.37 ± 0.04	6.29 ± 0.03	6.51 ± 0.04	5.00 ± 0.02	5.14 ± 0.04
6.44	4.77 ± 0.03	4.76 ± 0.04	5.58 ± 0.03	3.56 ± 0.04	4.34 ± 0.03	6.27 ± 0.03	6.50 ± 0.04	4.99 ± 0.02	5.13 ± 0.04
6.81	4.75 ± 0.03	4.76 ± 0.04	5.60 ± 0.03	3.58 ± 0.04	4.30 ± 0.04	6.26 ± 0.03	6.51 ± 0.04	4.96 ± 0.02	5.12 ± 0.04
7.17	4.71 ± 0.03	4.79 ± 0.04	5.59 ± 0.03	3.55 ± 0.04	4.23 ± 0.04	6.20 ± 0.04	6.48 ± 0.05	4.92 ± 0.03	5.11 ± 0.05
7.53	4.69 ± 0.03	4.76 ± 0.04	5.60 ± 0.03	3.50 ± 0.03	4.18 ± 0.03	6.15 ± 0.03	6.49 ± 0.04	4.88 ± 0.02	5.12 ± 0.04
7.89	4.65 ± 0.03	4.71 ± 0.04	5.59 ± 0.03	3.52 ± 0.03	4.22 ± 0.04	6.12 ± 0.04	6.48 ± 0.05	4.87 ± 0.02	5.13 ± 0.04
8.25	4.67 ± 0.03	4.76 ± 0.04	5.61 ± 0.03	3.55 ± 0.03	4.18 ± 0.04	6.17 ± 0.04	6.52 ± 0.05	4.90 ± 0.03	5.15 ± 0.04
8.61	4.72 ± 0.03	4.77 ± 0.03	5.61 ± 0.03	3.58 ± 0.04	4.25 ± 0.04	6.20 ± 0.03	6.50 ± 0.04	4.92 ± 0.02	5.14 ± 0.04
8.98	4.75 ± 0.04	4.74 ± 0.03	5.61 ± 0.03	3.59 ± 0.04	4.23 ± 0.04	6.21 ± 0.04	6.51 ± 0.04	4.92 ± 0.02	5.18 ± 0.04
9.34	4.74 ± 0.03	4.81 ± 0.03	5.61 ± 0.03	3.60 ± 0.03	4.21 ± 0.03	6.21 ± 0.04	6.49 ± 0.04	4.92 ± 0.02	5.16 ± 0.04
9.70	4.70 ± 0.03	4.79 ± 0.04	5.63 ± 0.03	3.56 ± 0.03	4.20 ± 0.04	6.19 ± 0.03	6.51 ± 0.04	4.90 ± 0.02	5.17 ± 0.04
10.06	4.67 ± 0.03	4.78 ± 0.03	5.64 ± 0.03	3.53 ± 0.04	4.13 ± 0.04	6.13 ± 0.03	6.52 ± 0.04	4.84 ± 0.02	5.18 ± 0.04
10.42	4.58 ± 0.04	4.76 ± 0.04	5.65 ± 0.03	3.48 ± 0.04	3.98 ± 0.04	6.01 ± 0.03	6.54 ± 0.05	4.75 ± 0.02	5.15 ± 0.04
10.79	4.48 ± 0.03	4.68 ± 0.04	5.66 ± 0.03	3.43 ± 0.04	3.72 ± 0.07	5.82 ± 0.03	6.51 ± 0.04	4.64 ± 0.02	5.12 ± 0.04
11.15	4.44 ± 0.03	4.74 ± 0.04	5.72 ± 0.03	3.39 ± 0.04	3.66 ± 0.09	5.72 ± 0.05	6.53 ± 0.04	4.52 ± 0.03	5.16 ± 0.04
11.51	4.42 ± 0.04	4.80 ± 0.03	5.76 ± 0.03	3.34 ± 0.04	3.47 ± 0.10	5.65 ± 0.05	6.52 ± 0.05	4.45 ± 0.03	5.18 ± 0.04
11.87	4.42 ± 0.04	4.81 ± 0.03	5.82 ± 0.03	3.24 ± 0.05	-	5.58 ± 0.05	6.53 ± 0.05	4.38 ± 0.03	5.17 ± 0.04
12.23	4.37 ± 0.03	4.78 ± 0.04	5.86 ± 0.04	3.26 ± 0.05	-	5.62 ± 0.05	6.52 ± 0.05	4.34 ± 0.02	5.17 ± 0.04
12.59	4.38 ± 0.04	4.76 ± 0.04	5.88 ± 0.03	3.26 ± 0.04	3.50 ± 0.12	5.54 ± 0.05	6.52 ± 0.03	4.28 ± 0.02	5.17 ± 0.04
12.96	4.33 ± 0.12	4.82 ± 0.04	5.90 ± 0.03	3.20 ± 0.05	3.43 ± 0.13	5.58 ± 0.05	6.49 ± 0.04	4.24 ± 0.03	5.13 ± 0.04
13.32	4.29 ± 0.04	4.73 ± 0.04	5.93 ± 0.02	3.22 ± 0.05	-	5.42 ± 0.07	6.47 ± 0.03	4.23 ± 0.03	5.14 ± 0.04

NOTE—Abundances in units of $12 + \log(X^{n+}/H^+)$